

DEUTSCHES ELEKTRONEN-SYNCHROTRON
Ein Forschungszentrum der Helmholtz-Gemeinschaft

DESY 12-159

September 2012

**Optimization of a dedicated bio-imaging
beamline at the European X-ray FEL**

Gianluca Geloni,
European XFEL GmbH, Hamburg

Vitali Kocharyan and Evgeni Saldin
Deutsches Elektronen-Synchrotron DESY, Hamburg

ISSN 0418-9833

NOTKESTRASSE 85 - 22607 HAMBURG

Optimization of a dedicated bio-imaging beamline at the European X-ray FEL

Gianluca Geloni,^{a,1} Vitali Kocharyan^b and Evgeni Saldin^b

^a*European XFEL GmbH, Hamburg, Germany*

^b*Deutsches Elektronen-Synchrotron (DESY), Hamburg, Germany*

Abstract

We recently proposed a basic concept for design and layout of the undulator source for a dedicated bio-imaging beamline at the European XFEL. The goal of the optimized scheme proposed here is to enable experimental simplification and performance improvement. The core of the scheme is composed by soft and hard X-ray self-seeding setups. Based on the use of an improved design for both monochromators it is possible to increase the design electron energy up to 17.5 GeV in photon energy range between 2 keV and 13 keV, which is the most preferable for life science experiments. An advantage of operating at such high electron energy is the increase of the X-ray output peak power. Another advantage is that 17.5 GeV is the preferred operation energy for SASE1 and SASE2 beamline users. Since it will be necessary to run all the XFEL lines at the same electron energy, this choice will reduce the interference with other undulator lines and increase the total amount of scheduled beam time. In this work we also propose a study of the performance of the self-seeding scheme accounting for spatiotemporal coupling caused by the use of a single crystal monochromator. Our analysis indicates that this distortion is easily suppressed by the right choice of diamond crystal planes and that the proposed undulator source yields about the same performance as in the case for a X-ray seed pulse with no coupling. Simulations show that the FEL power reaches 2 TW in the 3 keV - 5 keV photon energy range, which is the most preferable for single biomolecule imaging.

1 Introduction

The availability of free undulator tunnels at the European XFEL facility offers a unique opportunity to build a beamline optimized for coherent

¹ Corresponding Author. E-mail address: gianluca.geloni@xfel.eu

diffraction imaging of complex molecules, like proteins and other biologically interesting structures. Crucial parameters for such bio-imaging beamline are photon energy range, peak power, and pulse duration [1]-[4].

The highest diffraction signals are achieved at the longest wavelength that supports a given resolution, which should be better 0.3 nm. With photon energy of about 3 keV one can reach a resolution better than 0.3 nm with a detector designed to collect diffracted light in all forward directions, that is at angles $2\theta < \pi/2$. Higher photon energies up to about 13 keV give access to absorption edges of specific elements used for phasing by anomalous diffraction. The most useful edges to access are the K-edge of Fe (7.2 keV) and Se (12.6 keV), [5]. Access to the sulfur K-edge (2.5 keV) is required too. Finally, the users of the bio-imaging beamline also wish to investigate large biological structures in the soft X-ray photon energy range down to the water window (0.3 keV - 0.5 keV), [5].

Overall, one aims at the production of pulses containing enough photons to produce measurable diffraction patterns, and yet short enough to avoid radiation damage in a single pulse. This is, in essence, the principle of imaging by "diffraction before destruction" [2]. These capabilities can be obtained by reducing the pulse duration to 5 fs or less, and simultaneously increasing the peak power to the TW power level or higher, at photon energies between 3 keV and 5 keV, which are optimal for imaging of macromolecular structures [5].

The requirements for a dedicated bio-imaging beamline are the following. The X-ray beam should be delivered in ultrashort pulses with TW peak power and within a very wide photon energy range between 0.3 keV and 13 keV. The pulse duration should be adjustable from 10 fs in hard X-ray regime to 2 fs - 5 fs in photon energy range between 3 keV and 5 keV. At the European XFEL it will be necessary to run all undulator beamlines at the same electron energy and bunch charge. However, bio-imaging experiments should be performed without interference with other main SASE1, SASE2 beamlines. This assumes the use of nominal electron energy and electron beam distribution.

A key component of the bio-imaging beamline is the undulator source. A basic concept for layout and design of the undulator system for a dedicated bio-imaging beamline at the European XFEL was proposed in [6]. All the requirements in terms of photon beam characteristics can be satisfied by the use a very efficient combination of self-seeding, fresh bunch, and undulator tapering techniques [7]-[26], [27]-[30]. A combination of self-seeding and undulator tapering techniques would allow to meet the design TW output power. The bio-imaging beamline would be equipped with two different self-seeding setups, one provide monochromatization in the soft

X-ray range, and one to provide monochromatization in the hard X-ray range. The most preferable solution in the photon energy range for single biomolecule imaging consists in using a fresh bunch technique in combination with self-seeding and undulator tapering techniques. In [6] it was shown how the installation of an additional (fresh bunch) magnetic chicane behind the soft X-ray self-seeding setup enables an output power in the TW level for the photon energy range between 3 keV and 5 keV. Additionally, the pulse duration can be tuned between 2 fs and 10 fs with the help of this chicane, still operating with the nominal electron bunch distribution [31].

The overall setup proposed in [6] is composed of four undulators separated by three magnetic chicanes. The undulator parts consist of 4,3,4 and 29 cells. Each magnetic chicane compact enough to fit one 5 m-long undulator segment and the FODO lattice will not be perturbed. The undulator system will be realized in a similar fashion as other European XFEL undulators. In order to make use of standard components we favor the use of SASE3 type of undulator segments, which are optimized for the generation of soft X-rays. The present layout of the European XFEL enables to accommodate such new beamline. The previously proposed undulator source provides access to a photon energy range between 3 keV and 5 keV only at the reduced electron beam energy of 10.5 GeV. Although the 10.5 GeV is one of the nominal electron energy, it may not be the preferable mode of operation for SASE1, SASE2 beamline users. Note that the SASE3 undulator type would enable operation down to 0.7 keV at an electron energy of 17.5 GeV. However, the delay of photons induced in the grating monochromator (3 ps) and, consequently, the delay of the electrons required in the magnetic chicane of the soft X-ray self-seeding setup sets a limit to the electron energy.

This paper constitutes an update to the scheme proposed in [6]. The present design assumes the use of the same 40 cells undulator system, with an improved design of both self-seeding setups. To avoid any interference with other beamlines, we propose to extend the photon energy range of the self-seeding setup with a single crystal monochromator down to 3 keV [32]. As a result, the design electron energy can be increased up to 17.5 GeV in the photon energy range most preferable for bio-imaging. This is achieved exploiting 0.1 mm diamond crystals in symmetric Bragg geometry. Based on the use C(111), C(220), and C(400) reflections (σ -polarization) it will be possible to cover the photon energy range between 3 keV and 13 keV. In particular, we exploit C(111) reflection (σ -polarization) in photon energy range between 3 keV and 5 keV. Combination of self-seeding and fresh bunch techniques, as in the case of the original design, has the advantage that the pulse duration can be tuned between 2 fs and 10 fs.

The users of the bio-imaging beamline also wish to investigate their samples around sulfur K-edge, i.e. in the photon energy range between 2 keV and

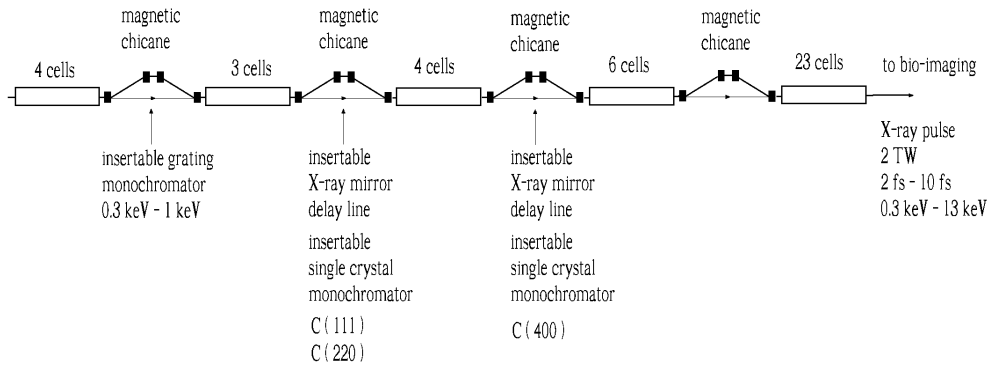


Fig. 1. Design of the undulator system for the bio-imaging beamline. The method exploits a combination of self-seeding, fresh bunch, and undulator tapering technique. Each magnetic chicane accomplishes three tasks by itself. It creates an offset for monochromator or X-ray mirror delay line installation, it removes the electron microbunching produced in the upstream undulator, and it acts as a magnetic delay line.

3 keV. A solution suitable for this spectral range constitutes a major challenge for self-seeding designers. In fact, on the one hand crystals with right lattice parameters are difficult to be obtained. On the other hand, grating monochromator throughput is usually too low due to high absorption. As for the original design we propose a method around this obstacle, which is based in essence on a fresh bunch technique, and exploits a self-seeding setup based on grating monochromator in the photon energy range between 0.7 keV and 1 keV. It should be noted that due to extension of the single crystal monochromator setup down to 3 keV, the maximal photon energy of operation for the grating monochromator is reduced from 1.7 keV in the original design down to 1 keV in the current design.

Also, here we adopt an improved design of grating monochromator, which was recently proposed for the soft X-ray self-seeding setup at the LCLS [33], substituting a previously proposed one [34, 35]. In this novel design the optical delay is reduced down to below 1 ps. As a result, a self-seeding setup with such grating monochromator allows for reduced constraints on the magnetic chicane, and can operate at the European XFEL down to 0.7 keV at the highest nominal electron energy of 17.5 GeV. Such high electron energy enables to increase the X-ray output peak power in the most preferable photon energy range for bio-imaging experiments up to 2 TW.

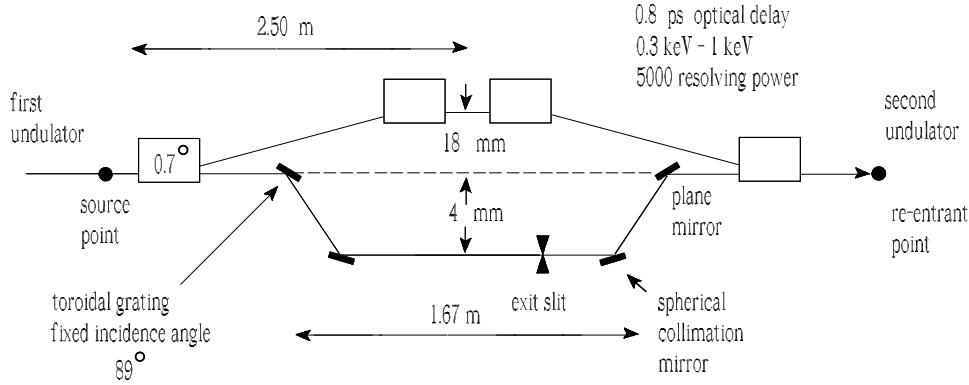


Fig. 2. Compact grating monochromator originally proposed at SLAC [33] for soft X-ray self-seeding setup. The chicane fits in one European XFEL undulator undulator section (5 m).

2 Setup description

Self-seeding is a promising approach to significantly narrow the SASE bandwidth and to produce nearly transform-limited X-ray pulses [14]-[24]. In its simplest configuration, a self-seeding setup in the hard X-ray regime consists of two undulators separated by photon monochromator and electron bypass beamline, typically a 4-dipole chicane. The two undulators are resonant at the same radiation wavelength. The SASE radiation generated by the first undulator passes through the narrow-band monochromator, thus generating a transform-limited pulse, which is then used as a coherent seed in the second undulator. Chromatic dispersion effects in the bypass chicane smear out the microbunching in the electron bunch produced by the SASE lasing in the first undulator. Electrons and monochromatized photon beam are recombined at the entrance of the second undulator, and the radiation is amplified by the electron bunch in the second undulator, until saturation is reached. The required seed power at the beginning of the second undulator must dominate over the shot noise power within the gain bandpass, which is order of a few kW.

Despite the unprecedented increase in peak power of the X-ray pulses for SASE X-ray FELs (see e.g. [36]), some applications, including single biomolecule imaging, require still higher photon flux. The most promising way to extract more FEL power than that at saturation is by tapering the magnetic field of the undulator [7]-[25]. Also, a significant increase in power is achievable by starting the FEL process from a monochromatic seed rather than from noise [21]-[24]. Tapering consists in a slow reduction of the field strength of the undulator in order to preserve the resonance wavelength,

while the kinetic energy of the electrons decreases due to the FEL process. The undulator taper could be simply implemented at discrete steps from one undulator segment to the next. The magnetic field tapering is provided by changing the undulator gap.

The setup suggested in this article constitutes an optimization of the original proposal in [6] and is composed of five undulator parts separated by four magnetic chicanes as shown in Fig. 1. These undulators consist of 4, 3, 4, 6 and 23 undulator cells, respectively. Each magnetic chicane is compact enough to fit one undulator segment. The installation of chicanes does not perturb the undulator focusing system. The implementation of the self-seeding scheme for soft X-ray would exploit the first magnetic chicane. The second and third magnetic chicanes create an offset for the installation of a single crystal monochromator or an X-ray mirror delay line, and act as a magnetic delay line. Both self-seeding setups should be compact enough to fit one undulator module.

For soft X-ray self-seeding, the monochromator usually consists of a grating [14]. Recently, a very compact soft X-ray self-seeding scheme has appeared, based on a grating monochromator [33]. The proposed monochromator is composed of a toroidal grating followed by three mirrors, and is equipped with an exit slit only. The delay of the photons is about 1 ps. The monochromator is continuously tunable in the photon energy range between 0.3 keV and 1 keV. The resolution is about 5000. The transmission of the monochromator beamline is close to 10%. The magnetic chicane delays the electron bunch accordingly, so that the photon beam passing through the monochromator system recombines with the same electron bunch. The chicane provides a dispersion strength of about 0.6 mm in order to match the optical delay and also smears out the SASE microbunching generated in the first 4 cells of the undulator. It should be noted that in [37] we studied the performance of a previous scheme of a grating monochromator for a soft X-ray self-seeding setup [34, 35]. For the present investigation we consider the new scheme in [33]. The layout of the bypass and of the monochromator optics is schematically shown in Fig. 2.

For hard X-ray self-seeding, a monochromator usually consists of crystals in the Bragg geometry. A conventional 4-crystal, fixed exit monochromator introduces optical delay of, at least, a few millimeters, which has to be compensated with the introduction of an electron bypass longer than one undulator module. To avoid this difficulty, a simpler self-seeding scheme was proposed in [20], which uses the transmitted X-ray beam from the single crystal to seed the same electron bunch. Here we propose to use a diamond crystal with a thickness of 0.1 mm. Using the symmetric C(400) Bragg reflection, it will be possible to cover the photon energy range from 7 keV to 9 keV, Fig. 3. The range between 5 keV and 7 keV can be covered

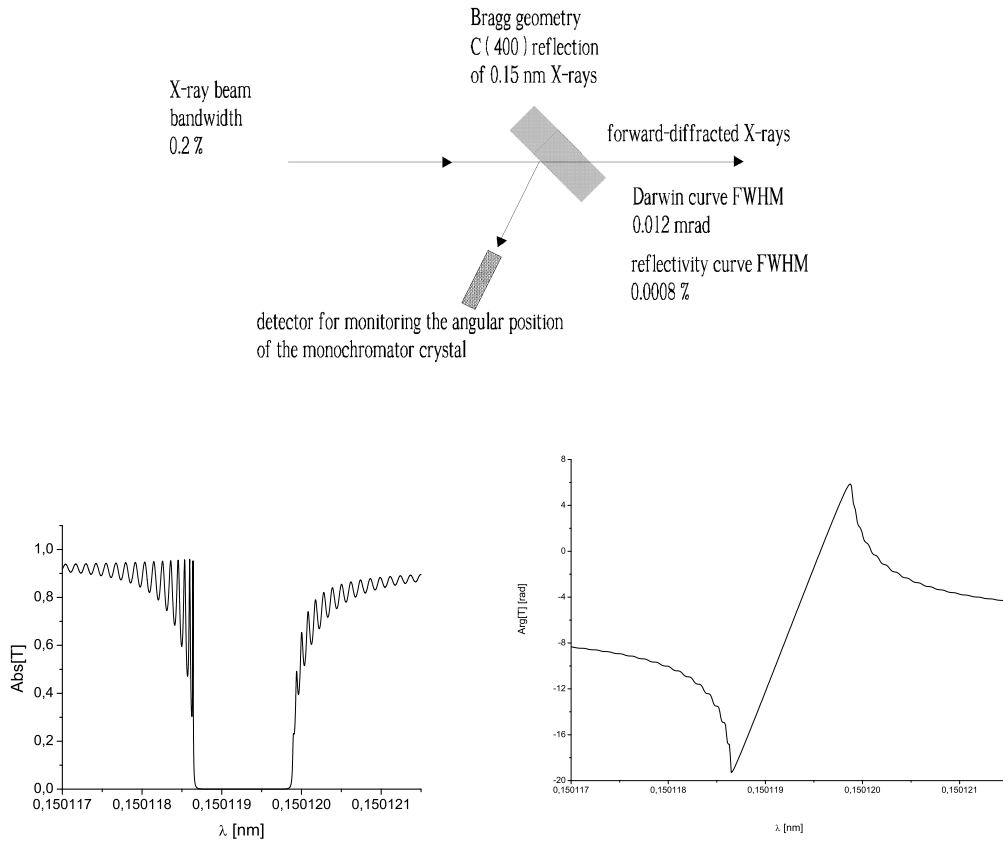


Fig. 3. X-ray optics for compact crystal monochromator originally proposed in [20] for a hard X-ray self-seeding setup, based on the C(400) reflection (σ -polarization). Modulus and phase of the transmissivity are shown in the two lower plots.

with the C(220) reflection, Fig. 4, while the range between 3 keV and 5 keV can be obtained using the C(111) reflection, Fig. 5.

One of the main technical problems for self-seeding designers is to provide bio-imaging capabilities in 2 keV - 3 keV photon energy range. Here we will use the same method already exploited in [6] to get around this obstacle. Our solution is based in essence on the fresh bunch technique [26] and exploits the above described conservative design of self-seeding setup based on a grating monochromator. The hardware requirement is minimal, and in order to implement a fresh bunch technique it is sufficient to install an additional magnetic chicane at a special position behind the soft X-ray self-seeding setup. The function of this second chicane is both to smear out the electron bunch microbunching, and to delay the electron bunch with respect to the monochromatic soft X-ray pulse produced in the second undulator. In this way, only half of the electron bunch is seeded, and saturates in the third undulator. Finally, the second half of the electron bunch, which remains unspoiled, is seeded by the third harmonic of the monochromatic radiation

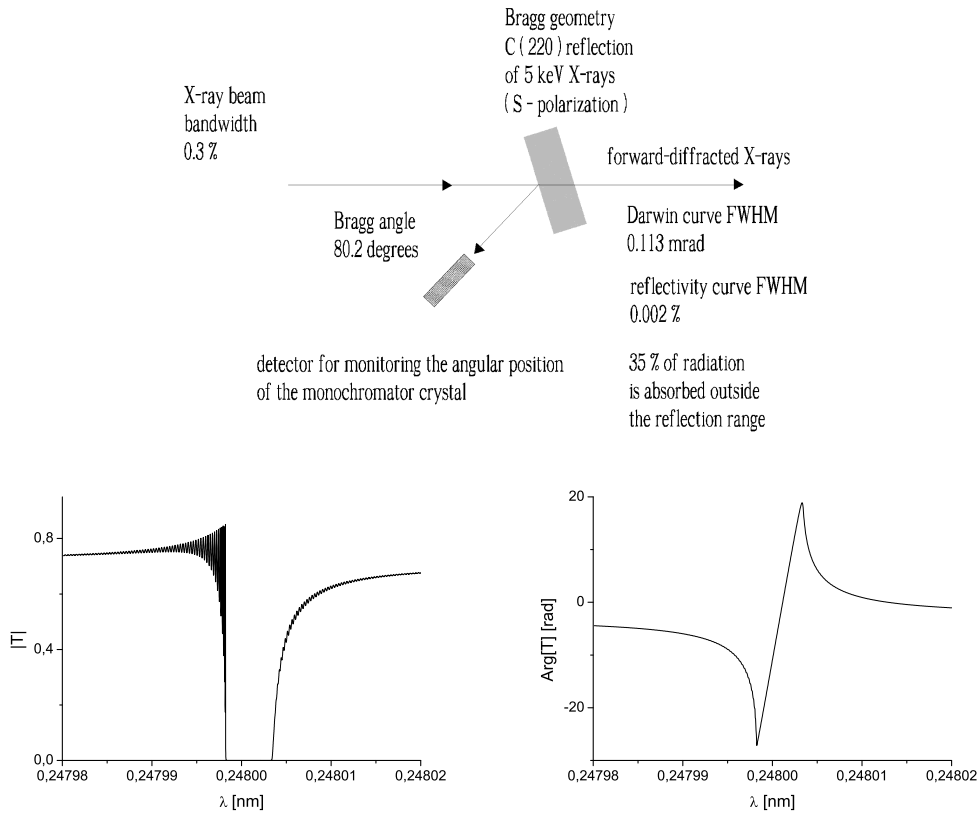


Fig. 4. Schematic of single crystal monochromator for operation in photon energy range between 5 keV and 7 keV. In this range the C(220) reflection will be exploited. Modulus and phase of the transmissivity are shown in the two lower plots.

pulse generated in the third undulator, which is also monochromatic. The final delay of the electron bunch with respect to the seed radiation pulse can be obtained with a third, hard X-ray self-seeding magnetic chicane, which in this mode of operation is simply used to provide magnetic delay. The monochromatic third harmonic radiation pulse used as seed for the unperturbed part of the electron bunch is in the GW power level, and the combination of self-seeding and fresh bunch technique is extremely insensitive to non-ideal effects. The final undulator, composed by 29 cells, is tuned to the third harmonic frequency, and is simply used to amplify the X-ray pulse up to the TW power level.

In order to introduce a tunable delay of the photon beam with respect to the electron beam, a mirror chicane can be installed within the second magnetic chicane, as shown in Fig. 6. The function of the mirror chicane is to delay the radiation in the range between 0.7 keV and 1 keV relatively to the electron bunch. The glancing angle of the mirrors is as small as 3 mrad. At the undulator location, the transverse size of the photon beam is smaller than 0.1 mm, meaning that the mirror length would be just about

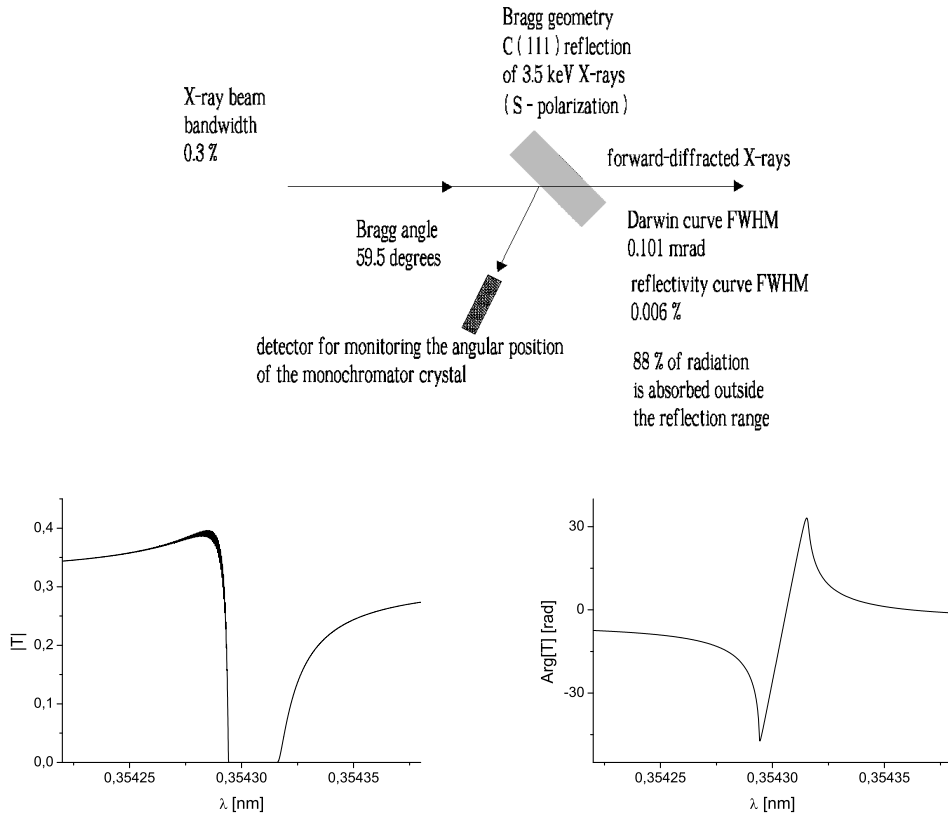


Fig. 5. Schematic of single crystal monochromator for operation in photon energy range between 3 keV and 5 keV. In this range the C(111) reflection will be exploited. Modulus and phase of the transmissivity are shown in the two lower plots.

5 cm. The single-shot mode of operation will relax the heat-loading issues. The mirror chicane can be built in such a way to obtain a delay of the radiation pulse of about $23 \mu\text{m}$. This is enough to compensate a bunch delay of about $20 \mu\text{m}$ from the magnetic chicane, and to provide any desired shift in the range between $0 \mu\text{m}$ and $3 \mu\text{m}$. Note that for the European XFEL parameters, 1 nm microbunching is washed out with a weak dispersive strength corresponding to an R_{56} in the order of ten microns. The dispersive strength of the proposed magnetic chicane is more than sufficient to this purpose. Thus, the combination of magnetic chicane and mirror chicane removes the electron microbunching produced in the second undulator and acts as a tunable delay line within $0 \mu\text{m}$ and $3 \mu\text{m}$ with the required choice of delay sign.

2.1 Operation into the water window

The five-undulator configuration in Fig. 1 can be naturally taken advantage of at different photon energies ranging from soft to hard X-rays. Fig. 7 shows

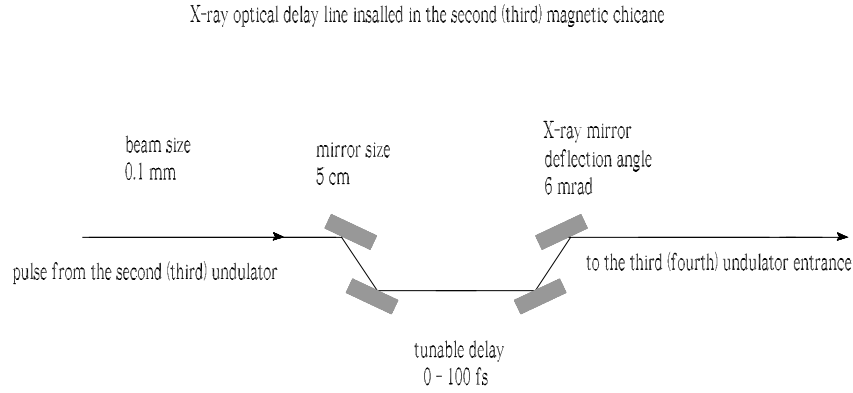


Fig. 6. X-ray optical system for delaying the soft X-ray pulse with respect to the electron bunch. Two distinct X-ray optical systems can be installed within the second and the third magnetic chicane.

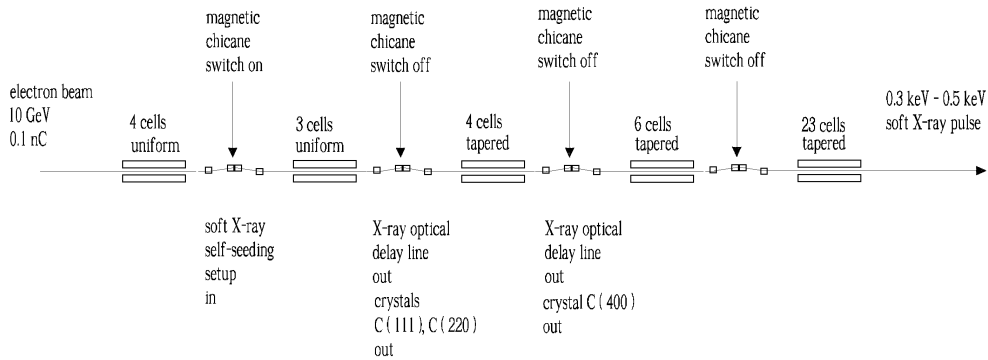


Fig. 7. Design of the undulator system for high power mode of operation in the water window. The method exploits a combination of self-seeding scheme with grating monochromator and an undulator tapering technique.

the basic setup for the high-power mode of operation in the soft X-ray wavelength range. The second, the third and the fourth chicane are not used for such regime, and must be switched off. After the first undulator (4 cells-long) and the grating monochromator, the output undulator follows. The first section of the output undulator (consisting of second and third undulator) is composed by 3 untapered cells, while tapering is implemented starting from the second cell of the fourth undulator. The monochromatic seed is exponentially amplified by passing through the first untapered section of the output undulator. This section is long enough to allow for saturation, and yields an output power of about 100 GW. Such monochromatic FEL output is finally enhanced up to 1 TW in the second output-undulator section, by

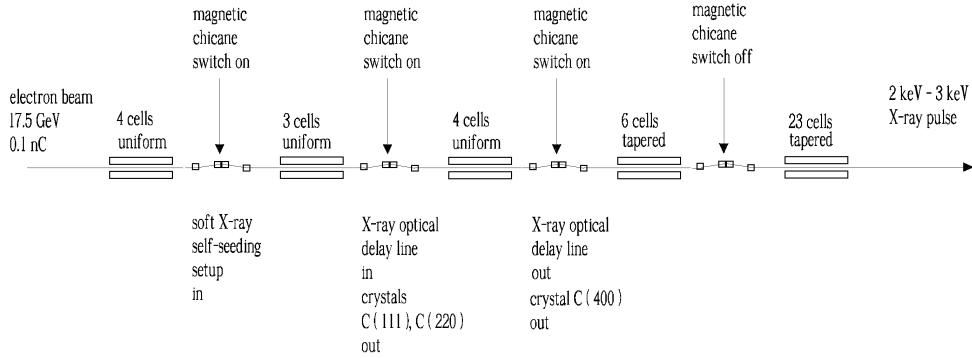


Fig. 8. Design of the undulator system for high power mode of operation around the sulfur K-edge. The method exploits a combination of self-seeding scheme with grating monochromator, fresh bunch and undulator tapering techniques.

tapering the undulator parameter over the last cells after saturation. Under the constraints imposed by undulator and chicane parameters it is only possible to operate at the nominal electron beam energy of 10.5 GeV. The setup was optimized based on results of start-to-end simulations for a nominal electron beam with 0.1 nC charge. Results were presented in [37], where we studied the performance of this scheme for the SASE3 upgrade.

2.2 Operation around the sulfur K-edge

Fig. 8 shows the basic setup for high power mode of operation in the photon energy range between 2 keV and 3 keV. The first three chicanes are used for such regime, and must be switched on, while the last fourth chicane is off. The third chicane is used as a magnetic delay only, and the crystal must be removed from the light path. We propose to perform monochromatization at photon energies ranging between 0.7 keV and 1 keV with the help of a grating monochromator, and to amplify the seed in the second undulator up to the power level of 0.2 GW. The second chicane smears out the electron microbunching and delays the monochromatic soft X-ray pulse of $2 \mu\text{m}$ with respect to the electron bunch. In this way, half of the electron bunch is seeded and saturates in the third undulator up to 40 GW. At saturation, the electron beam generates considerable monochromatic radiation at the third harmonic in the GW power level. The third magnetic chicane smears out the electron microbunching and delays the electron bunch with respect to the radiation of $2 \mu\text{m}$. Thus, the unspoiled part of the electron bunch is seeded by the GW-level monochromatic pulse at the third harmonic frequency, Fig. 10. The fourth, 29 cells-long undulator is tuned to the third harmonic

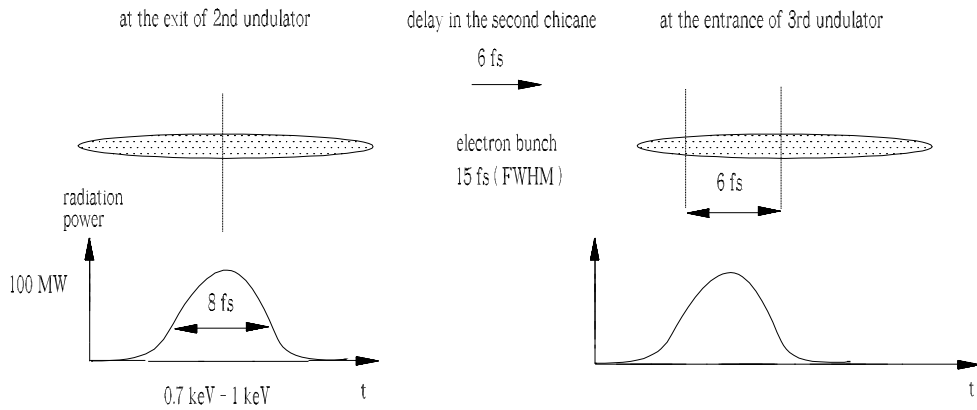


Fig. 9. Principle of the fresh bunch technique for the high power mode of operation in the photon energy range between 2 keV and 3 keV. The second chicane smears out the electron microbunching and delays the monochromatic soft X-ray pulse with respect to the electron bunch of 6 fs. In this way, half of the electron bunch is seeded and saturates in the third undulator.

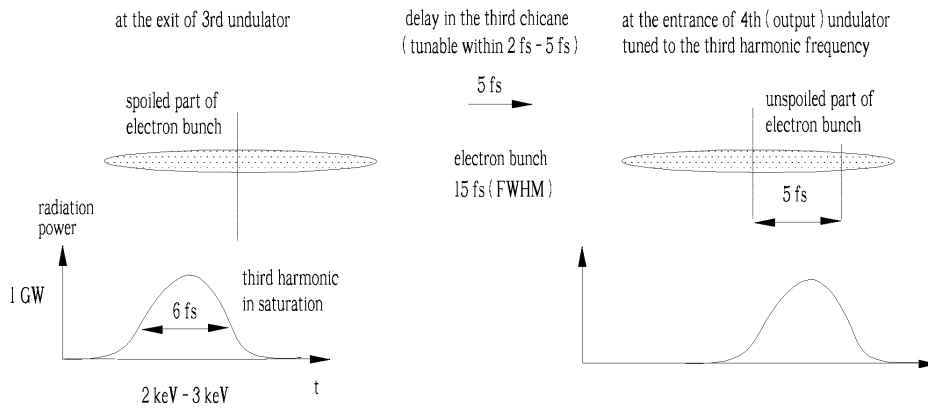


Fig. 10. Principle of the fresh bunch technique for the high power mode of operation in the photon energy range between 2 keV and 3 keV. The third magnetic chicane smears out the electron microbunching and delays the electron bunch with respect to the radiation pulse. The unspoiled part of electron bunch is seeded by a GW level monochromatic pulse at third harmonic frequency. Tunability of the output pulse duration can be easily obtained by tuning the magnetic delay of the third chicane.

frequency (between 2 keV and 3 keV), and is used to amplify the radiation pulse up to 1 TW. The additional advantage of the proposed setup for bio-imaging is the tunability of the output pulse duration, which is obtained by tuning the magnetic delay of the third chicane. Simulations show that the X-ray pulse duration can be tuned from 2 fs to 5 fs. The production of such pulses is of great importance when it comes to single biomolecule imaging experiments.

The soft X-ray background can be easily eliminated by using a spatial window positioned downstream of the fourth undulator exit [6]. Since the soft X-ray radiation has an angular divergence of about 0.02 mrad FWHM, and the slits are positioned more than 100 m downstream of the third undulator, the background has much larger spot size compared with the 2 keV - 3 keV radiation spot size, which is about 0.1 mm at the exit of the fourth undulator. Therefore, the background radiation power can be diminished of more than two orders of magnitude without any perturbations of the main pulse.

With the monochromator design in [33], it will be possible to operate at an electron beam energy of 17.5 GeV. The setup was optimized based on results from start-to-end simulations for a nominal electron bunch with a charge of 0.1 nC. Results are presented in the following Sections of this article. The proposed undulator setup uses the electron beam coming from the SASE1 undulator. We assume that SASE1 operates at the photon energy of 12 keV, and that the FEL process is switched off for one single dedicated electron bunch within each macropulse train. A method to control the FEL amplification process is based on the betatron switcher technique described in [38, 39]. Due to quantum energy fluctuations in the SASE1 undulator, and to wakefields in the SASE1 undulator pipe, the energy spread and the energy chirp of the electron bunch at the entrance of the bio-imaging beamline significantly increase compared with the same parameters at the entrance of the SASE1 undulator. The dispersion strength of the first chicane has been taken into account from the viewpoint of the electron beam dynamics, because it disturbs the electron beam distribution. The other two chicanes have tenfold smaller dispersion strength compared with the first one. The electron beam was tracked through the first chicane using the code Elegant [40]. The electron beam distortions complicate the simulation procedure. However, simulations show that the proposed setup is not significantly affected by perturbations of the electron phase space distribution, and yields about the same performance as in the case for an electron beam without the tracking through the first chicane (see below).

2.3 Operation in the 3 keV - 7 keV photon energy range

Starting with the energy range of 3 keV it is possible to use a single crystal monochromator instead of a grating monochromator at an electron energy of 17.5 GeV. Different crystal reflections and different positions of the monochromator down the undulator enable self-seeding for different spectral ranges.

For the range between 3 keV and 5 keV, Fig. 11, the first chicane is not used and is switched off. After the first 7 cells the electron and the photon beams

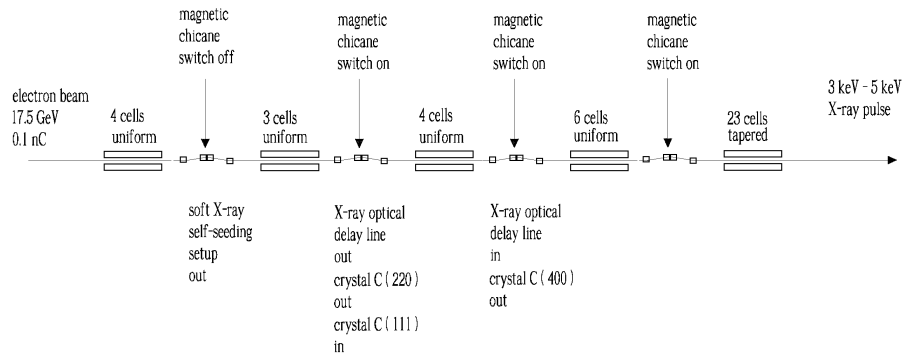


Fig. 11. Design of the undulator system for high power mode of operation in the most preferable photon energy range for single molecule imaging, between 3 keV and 5 keV. The method exploits a combination of the self-seeding scheme with single crystal monochromator, fresh bunch and undulator tapering techniques.

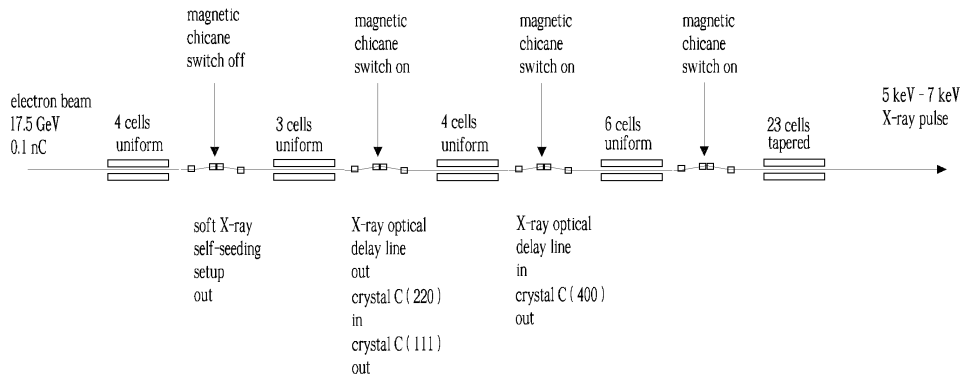


Fig. 12. Design of the undulator system for high power mode of operation in the photon energy range between 5 keV and 7 keV. The method exploits a combination of self-seeding scheme with single crystal monochromator, fresh bunch and undulator tapering techniques.

are separated with the help of the second magnetic chicane, and the C(111) reflection is used to monochromatize the radiation. The seed is amplified in the next 4 cells. After that, the electron and the photon beam are separated again by the third chicane, and an X-ray optical delay line allows for the introduction of a tunable delay of the photon beam with respect to the electron beam. The following 6 cells use only a part of the electron beam as a lasing medium. A magnetic chicane follows, which shifts the unspoiled part of the electron bunch on top of the of the photon beam. In this way, a fresh bunch technique can be implemented. Since the delays are tunable,

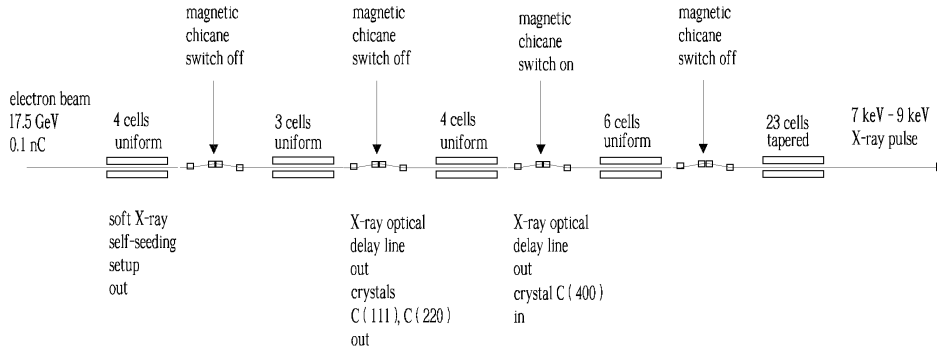


Fig. 13. Design of the undulator system for high power mode of operation in the photon energy range in the photon energy range between 7 keV and 9 keV. The method exploits a combination of self-seeding scheme with single crystal monochromator and an undulator tapering technique.

the photon pulse length can also be tuned. Finally, radiation is amplified into the last 23 tapered cells to provide pulses with about 2 TW power. The photon energy range between 5 keV and 7 keV can be achieved similarly, Fig. 12. The only difference is that now the C(220) reflection is used, instead of the C(111).

It may be worth to point out the difference between the operation in the 3 keV - 7 keV range and the previously discussed range between 2 keV and 3 keV. In the 3 keV - 7 keV range we use seeding in combination of a fresh bunch technique, but we do not exploit harmonic generation. Moreover, the fresh bunch technique is only used for tuning the duration of the radiation pulse.

2.4 Operation in the 7 keV - 9 keV photon energy range

The energy range between 7 keV and 9 keV can be achieved by deactivating the first and the second magnetic chicane, thus letting the SASE process building up the radiation pulse to be monochromatized for 11 cells. After that, the third chicane is used for the monochromator setup, which makes use of the C(400) reflection. The last chicane is switched off, and the the output undulator is long enough to reach 1 TW power. The duration of the output pulses is of about 10 fs. If tunability of the pulse duration is requested in this energy range, this is most easily achieved by providing additional delay with the fourth magnetic chicane installed behind the hard X-ray self-seeding setup.

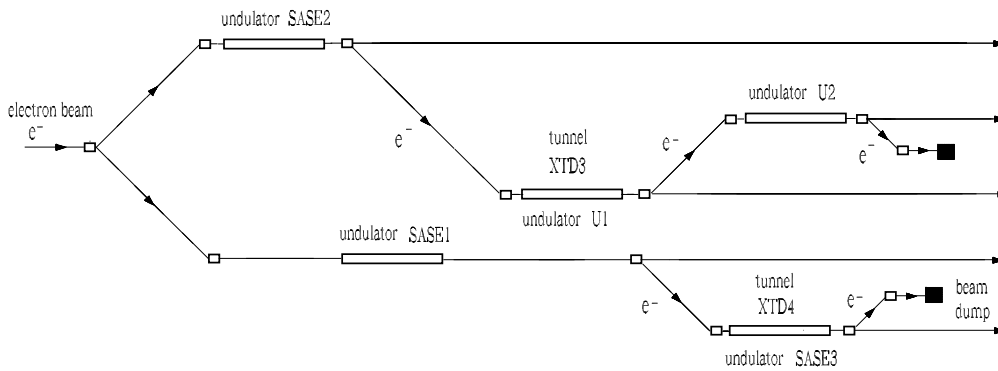


Fig. 14. Original design of the European XFEL facility.

2.5 Operation around the selenium K-edge

Finally, for the energy range between 9 keV and 13 keV, a combination of self-seeding, fresh bunch technique and harmonic generation is used. The undulator line is configured as for the range between 3 keV and 5 keV, Fig. 11, the only difference being that the final undulator segments are tuned at the third harmonic of the fundamental thus enabling the 9 keV - 13 keV energy range. As before, the first chicane is not used and is switched off. After the first 7 cells the electron and the photon beams are separated with the help of the second magnetic chicane, and the C(111) reflection is used to monochromatize the radiation. The seed is amplified in the next 4 cells. After that, the electron and the photon beam are separated again by the third chicane, and an X-ray optical delay line allows for the introduction of a tunable delay of the photon beam with respect to the electron beam. The second chicane smears out the electron microbunching and delays the monochromatic soft X-ray pulse with respect to the electron bunch of 6 fs. In this way, half of the electron bunch is seeded and saturates in the following 6 cells. A magnetic chicane follows, which shifts the unspoiled part of the electron bunch on top of the photon beam. In this way, a fresh bunch technique can be implemented. Since the delays are tunable, the photon pulse length can also be tuned. Since third harmonic bunching is considerable, the last 23 tapered cells are tuned at the third harmonic of the fundamental providing pulses with about 0.5 TW power.

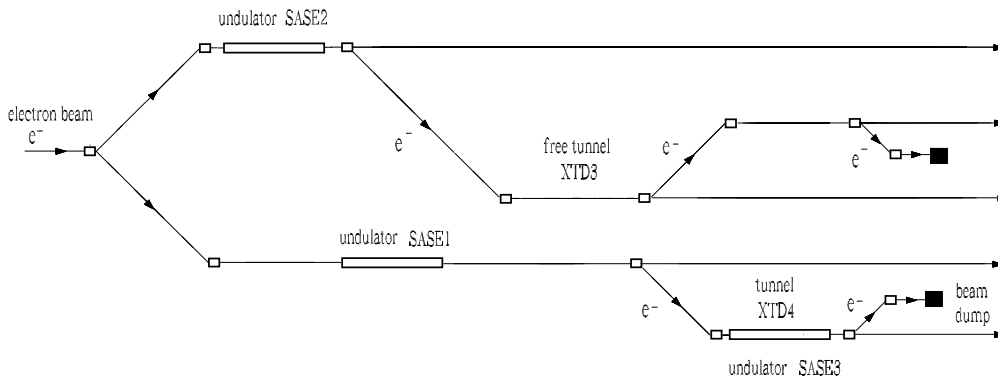


Fig. 15. Current design of the European XFEL facility.

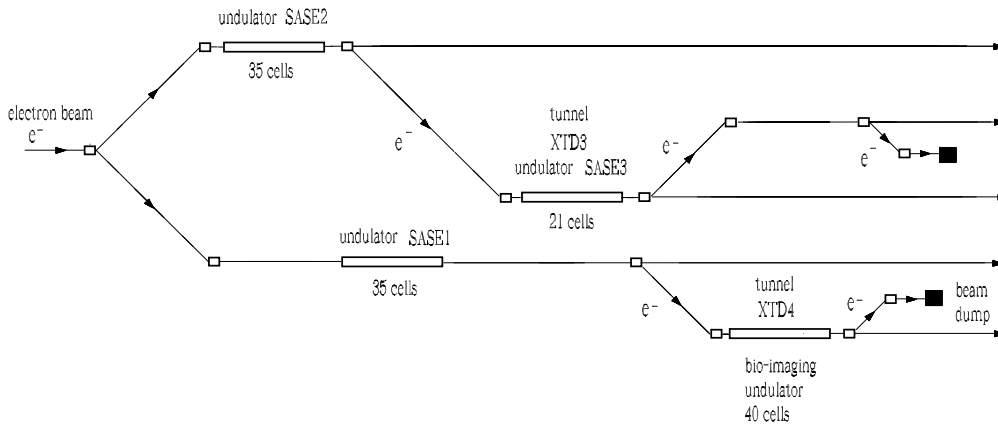


Fig. 16. Schematic of the proposed extension of the European XFEL facility.

2.6 Possible location of the bio-imaging line

The original design of the European XFEL [41] was optimized to produce XFEL radiation at 0.1 nm, simultaneously at two undulator lines, SASE1 and SASE2. Additionally, the design included one FEL line in the soft X-ray range, SASE3, and two undulator lines for spontaneous synchrotron radiation, U1 and U2, Fig. 14. The soft X-ray SASE3 beamline used the spent electron beam from SASE1, and the U1 and U2 beamlines used the spent beam from SASE2. In fact, although the electron beam performance is degraded by the FEL process, the beam can still be used in afterburner mode in the SASE3 undulator, which will be equipped with a 126 m-long undulator system, for a total of 21 cells.

After a first design report, the layout of the European XFEL changed. In the

last years after the achievement of the LCLS, and the subsequent growth of interest in XFEL radiation by the scientific community, it became clear that the experiments with XFEL radiation, rather than with spontaneous synchrotron radiation, had to be prioritized. In the new design, the two beamlines behind SASE2 are now free for future XFEL undulators installations, Fig. 15.

Recently it was also realized that the amplification process in the XFEL undulators can be effectively controlled by betatron FEL switchers [38, 39]. The SASE3 undulator was then optimized for generating soft X-rays. However, due to the possibility of switching the FEL process in SASE1, it is possible to produce high power SASE3 radiation in a very wide photon energy range between 0.3 keV and 13 keV. The SASE3 beamline is now expected to provide excellent performance, and to take advantage of its location in the XTD4 tunnel, which is close to the experimental hall and has sufficient free space behind the undulator for future expansion (140 m). After this section, the electron beam will be separated from the photon beam and will be bent down to an electron beam dump, Fig. 14. In the photon energy range between 3 keV and 13 keV, the SASE3 beamline is now expected to provide even better conditions for users than SASE1 and SASE2.

In this article we propose to build the bio-imaging beamline in the XTD4 tunnel. The SASE3 undulator, which is composed by 21 cells, can be installed from the very beginning in the free XTD3 tunnel, which is shorter than the XTD4 tunnel but sufficiently long for such installation, Fig. 16. The undulator can be placed within the straight beam path that is defined by the last upstream and first downstream dipole of the electron deflection system. The limiting length given by these constraints is referred to as "available length". For the XTD3 and the XTD4 tunnels this available length respectively amounts to 255 m and 460 m, see [42]. However, the electron beam optics requires sufficient space in front and the above-mentioned dipoles. The length that fits these electron optics restrictions is referred to as "potential length" and can be actually used for installations. For the XTD3 and the XTD4 tunnels, this potential length respectively amounts to 215 m and 400 m [42]. It should be mentioned that the potential length of the XTD4 tunnel is practically the same as the main SASE1 and SASE2 tunnels, and nicely fits with the undulator system for a dedicated bio-imaging beamline. It offers thus a great potential for future upgrades of this new beamline.

The bio-imaging beamline would support experiments carried out over a rather wide photon energy range. It is therefore proposed that the photon beam transport of the new beamline includes two lines. Line A uses 0.5m-long mirrors operating at a grazing angle of 2 mrad. This line is dedicated to the transport of X-ray radiation in the photon energy range from 3 keV up to 13 keV. This would be complementary to the Line B that is now optimized

in the soft X-ray range between 0.3 keV and 3 keV. The distance from the 40-cells-long undulator exit to the first mirror system will be only of about 100m^2 .

3 Spatiotemporal transformation caused by the use of a single crystal monochromator

The development of self-seeding schemes in the hard X-ray wavelength range necessarily involves crystal monochromators. Any device like a crystal monochromator introduces spatiotemporal deformations of the seeded X-ray pulse, which can be problematic for seeding. The spatiotemporal coupling in the electric field relevant to self-seeding schemes with crystal monochromators has been analyzed in the frame of classical dynamical theory of X-ray diffraction [43]. This analysis shows that a crystal in Bragg reflection geometry transforms the incident electric field $E(x, t)$ in the $\{x, t\}$ domain into $E(x - at, t)$, that is the field of a pulse with a less well-known distortion, first studied in [44]. The physical meaning of this distortion is that the beam spot size is independent of time, but the beam central position changes as the pulse evolves in time. Here we show in a simple manner that, based on the use only Bragg law, we may arrive directly to explanation of spatiotemporal coupling phenomena in the dynamical theory of X-ray diffraction [45].

Let us consider an electromagnetic plane wave in the X-ray frequency range incident on an infinite, perfect crystal. Within the kinematical approximation, according to the Bragg law, constructive interference of waves scattered from the crystal occurs if the angle of incidence, θ_i and the wavelength, λ , are related by the well-known relation

$$\lambda = 2d \sin \theta_i . \tag{1}$$

assuming reflection into the first order. This equation shows that for a given wavelength of the X-ray beam, diffraction is possible only at certain angles determined by the interplanar spacings d . It is important to remember the following geometrical relationships:

1. The angle between the incident X-ray beam and normal to the reflection

² This is in contrast with SASE1 and SASE2 beamlines, where an opening angle of 0.003 mrad at 3 keV FEL radiation leads to unacceptable mirror length of 2 m due to long distance of about 500 m between the source and mirror system. For these beamlines there is no possibility to use identical configuration of mirrors within the photon energy range from 3 keV to 13 keV.

plane is equal to that between the normal and the diffracted X-ray beam. In other words, Bragg reflection is a mirror reflection, and the incident angle is equal to the diffracted angle ($\theta_i = \theta_D$).

2. The angle between the diffracted X-ray beam and the transmitted one is always $2\theta_i$. In other words, incident beam and forward diffracted (i.e. transmitted) beam have the same direction.

We now turn our attention beyond the kinematical approximation to the dynamical theory of X-ray diffraction by a crystal. An optical element inserted into the X-ray beam is supposed to modify some properties of the beam as its width, its divergence, or its spectral bandwidth. It is useful to describe the modification of the beam by means of a transfer function. The transmissivity curve - the transmittance - in Bragg geometry can be expressed in the frame of dynamical theory as

$$T(\theta_i, \omega) = T(\Delta\omega + \omega_B \Delta\theta \cot \theta_B), \quad (2)$$

where $\Delta\omega = (\omega - \omega_B)$ and $\Delta\theta = (\theta_i - \theta_B)$ are the deviations of frequency and incident angle of the incoming beam from the Bragg frequency and Bragg angle, respectively. The frequency ω_B and the angle θ_B are given by the Bragg law: $\omega_B \sin \theta_B = \pi c/d$. Here we followed the usual procedure of expanding ω in a Taylor series about ω_B , so that

$$\omega = \omega_B + (d\omega/d\theta)_B(\theta - \theta_B) + \dots \quad (3)$$

Consider now a perfectly collimated, white beam incident on the crystal. In kinematical approximation T is a Dirac δ -function, which is simply represented by the differential form of Bragg law:

$$d\lambda/d\theta_i = \lambda \cot \theta_i. \quad (4)$$

In contrast to this, in dynamical theory the reflectivity width is finite. This means that there is a reflected beam even when incident angle and wavelength of the incoming beam are not related exactly by Bragg equation. It is interesting to note that the geometrical relationships 1. and 2. are still valid in the framework of dynamical theory. In particular, reflection in dynamical theory is always a mirror reflection. We underline here that if we have a perfectly collimated, white incident beam, we also have a perfectly collimated reflected and transmitted beam. Its bandwidth is related with the width of the reflectivity curve. We will regard the beam as perfectly collimated when the angular spread of the beam is much smaller than the angular width of the transfer function T . It should be realized that the crystal does not

introduce an angular dispersion similar to a grating or a prism. However, a more detailed analysis based on the expression for the reflectivity, Eq. (2), shows that a less well-known spatiotemporal coupling exists. The fact that the reflectivity is invariant under angle and frequency transformations obeying

$$\Delta\omega + \omega_B \Delta\theta \cot \theta_B = \text{const} \quad (5)$$

is evident, and corresponds to the coupling in the Fourier domain $\{k_x, \omega\}$. The origin of this relation is kinematical, in the sense that it follows from Bragg diffraction. One might be surprised that the field transformation derived in [43] for an XFEL pulse after a crystal in the $\{x, t\}$ domain is given by

$$E_{\text{out}}(x, t) = FT[T(\Delta\omega, k_x)E_{\text{in}}(\Delta\omega, k_x)] = E(x - ct \cot \theta_B, t), \quad (6)$$

where FT indicates a Fourier transform from the $\{k_x, \omega\}$ to the $\{x, t\}$ domain, and $k_x = \omega_B \Delta\theta / c$. In general, one would indeed expect the transformation to be symmetric in both the $\{k_x, \omega\}$ and in the $\{x, t\}$ domain due to the symmetry of the transfer function³. However, it is reasonable to expect the influence of a nonsymmetric input beam distribution. In the self-seeding case, the incoming XFEL beam is well collimated, meaning that its angular spread is a few times smaller than angular width of the transfer function. Only the bandwidth of the incoming beam is much wider than the bandwidth of the transfer function. In this limit, we can approximate the transfer function in the expression for the inverse temporal Fourier transform as a Dirac δ -function. This gives

$$\begin{aligned} E_{\text{out}}(x, t) &= FT[R(\Delta\omega, k_x)E_{\text{in}}(\Delta\omega, k_x)] \\ &= \xi(t) \cdot \frac{1}{2\pi} \int dk_x \exp(-ik_x ct \cot \theta_B) \exp(ik_x x) E_{\text{in}}(0, k_x) \\ &= \xi(t) b(x - ct \cot \theta_B), \end{aligned} \quad (7)$$

where we applied the Shift Theorem twice, and where

$$\xi(t) = \frac{1}{2\pi} \int dY \exp(iYt) R(Y) \quad (8)$$

is the inverse temporal Fourier transform of the reflectivity curve.

³ There is a breaking of the symmetry in the diffracted beam in the $\{k_x, \omega\}$ domain. While the symmetry is present at the level of the transfer function, it is not present anymore when one considers the incident beam. We point out that symmetry breaking in [43] is a result of the approximation of temporal profile of the incident wave to a Dirac δ -function.

Table 1
Undulator parameters

	Units	
Undulator period	mm	68
Periods per cell	-	73
Total number of cells	-	40
Intersection length	m	1.1
Photon energy	keV	0.3-13

The spatial shift given by Eq. (6) is proportional to $\cot(\theta_B)$, and is maximal in the range for small θ_B . If we want to use long delay $ct \sim 15\mu\text{m}$, a rms transverse size of radiation pulse of about $15\mu\text{m}$ limits the maximum acceptable value of $\cot(\theta_b)$ to 1 – 1.5. Thus, the spatiotemporal coupling is an issue, and efforts are necessarily required to avoid distortion. It is worth mentioning that this distortion is easily suppressed by the right choice of crystal planes.

4 FEL studies

With reference to Fig. 1 we performed feasibility studies pertaining different energy ranges considered in this article. These studies were performed with the help of the FEL code GENESIS 1.3 [46] running on a parallel machine. Simulations are based on a statistical analysis consisting of 100 runs.

The main undulator parameters are reported in Table 1. Operation is foreseen at two different energies: 10.5 GeV and 17.5 GeV. The lower energy is used in the very soft X-ray regime, between 0.3 keV and 0.5 keV. For this case, we refer to [37] for a summary of the electron beam characteristics at the entrance of the setup. The case for 17.5 GeV instead is summarized in Fig. 17, where we plot the results of start-to-end simulations [31].

4.1 Soft X-ray photon energy range

Production of soft X-rays with photon energies below 1 keV is enabled by configuring the setup as described in Fig. 7. A feasibility study for this case has been already carried out in [37], to which we refer the reader for further details and simulation results.

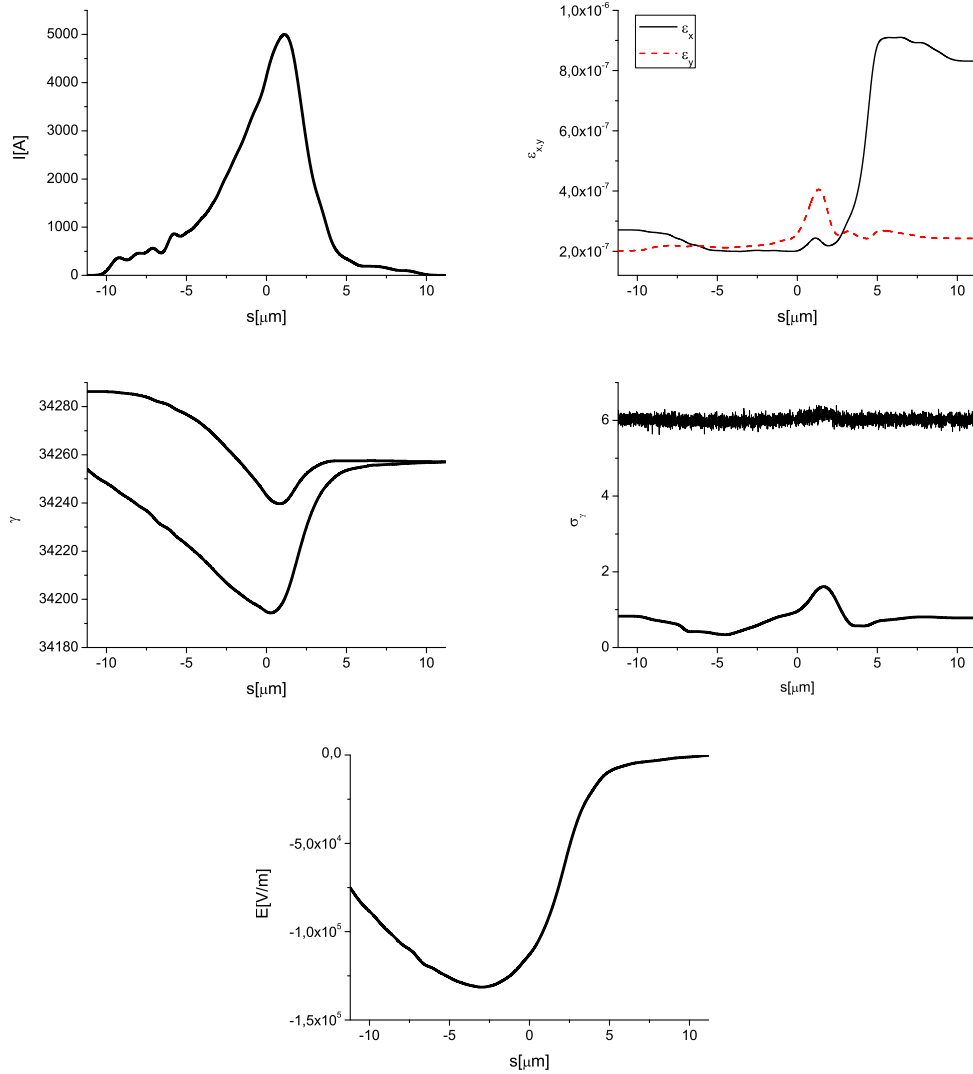


Fig. 17. Results from electron beam start-to-end simulations at the entrance of the undulator system of the bio-imaging beamline [31] for the hard X-ray case for the 17.5 GeV mode of operation. (First Row, Left) Current profile. (First Row, Right) Normalized emittance as a function of the position inside the electron beam. (Second Row, Left) Energy profile along the beam, lower curve. The effects of resistive wakefields along SASE1 are illustrated by the comparison with the upper curve, referring to the entrance of SASE1 (Second Row, Right) Electron beam energy spread profile, upper curve. The effects of quantum diffusion along SASE1 are illustrated by the comparison with the lower curve, referring to the entrance of SASE1. (Bottom row) Resistive wakefields in the SASE3 undulator [31].

4.2 Photon energy range between 2 keV and 3 keV

We now turn to analyze the case described in Fig. 8, which pertains the energy range between 2 keV and 3 keV. The electron beam energy here is

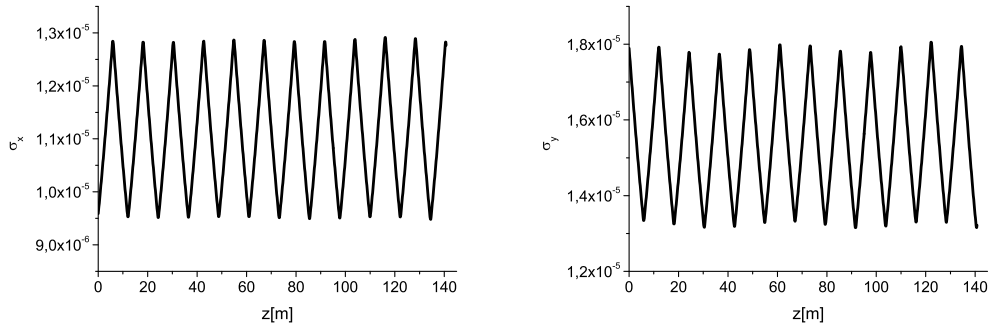


Fig. 18. Evolution of the horizontal (left plot) and vertical (right plot) dimensions of the electron bunch as a function of the distance inside the undulator. The plots refer to the longitudinal position inside the bunch corresponding to the maximum current value.

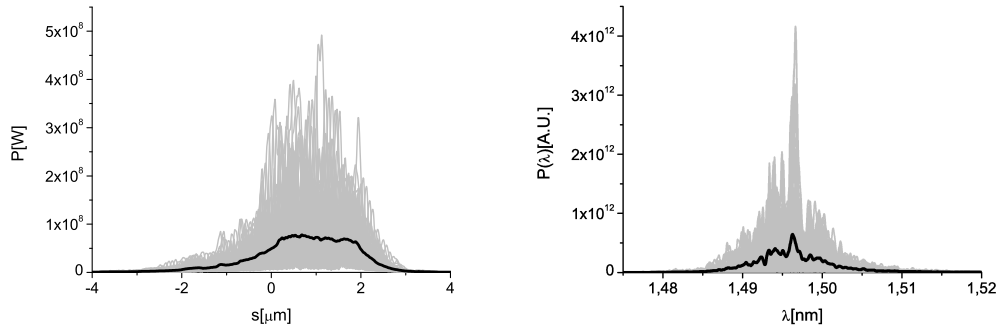


Fig. 19. Power and spectrum before the first magnetic chicane. Grey lines refer to single shot realizations, the black line refers to the average over a hundred realizations.

17.5 GeV.

The expected beam parameters at the entrance of the bio-imaging beamline undulator, and the resistive wake inside the undulator are shown in Fig. 17. The evolution of the transverse electron bunch dimensions are plotted in Fig. 18. Since the electron energy is fixed to 17.5 GeV, both expected beam parameters and evolution of the transverse beam dimensions before the tapered part are valid for the different energy ranges treated in the following Sections.

We begin our investigation by simulating the SASE power and spectrum after the first 4 undulator cells, that is before the first magnetic chicane. Results are shown in Fig. 19.

The magnetic chicane is switched on, and the soft X-ray monochromator is inserted. Assuming a monochromator efficiency of 10%, a Gaussian line, and a resolving power of 5000 we can filter the incoming radiation pulse in

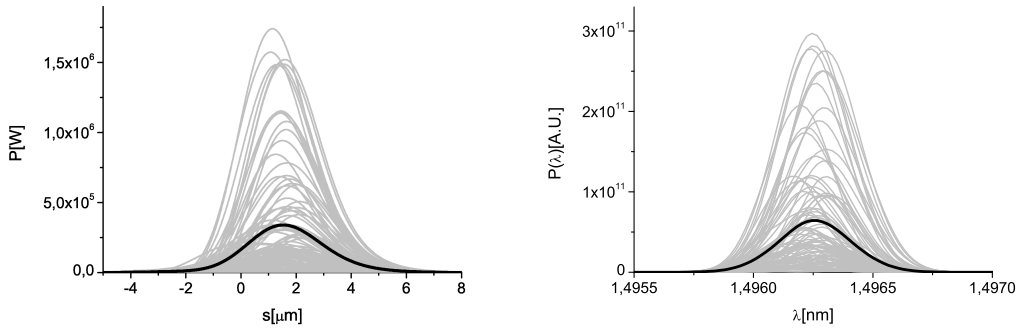


Fig. 20. Power and spectrum after the first magnetic chicane and soft X-ray monochromator. Grey lines refer to single shot realizations, the black line refers to the average over a hundred realizations.

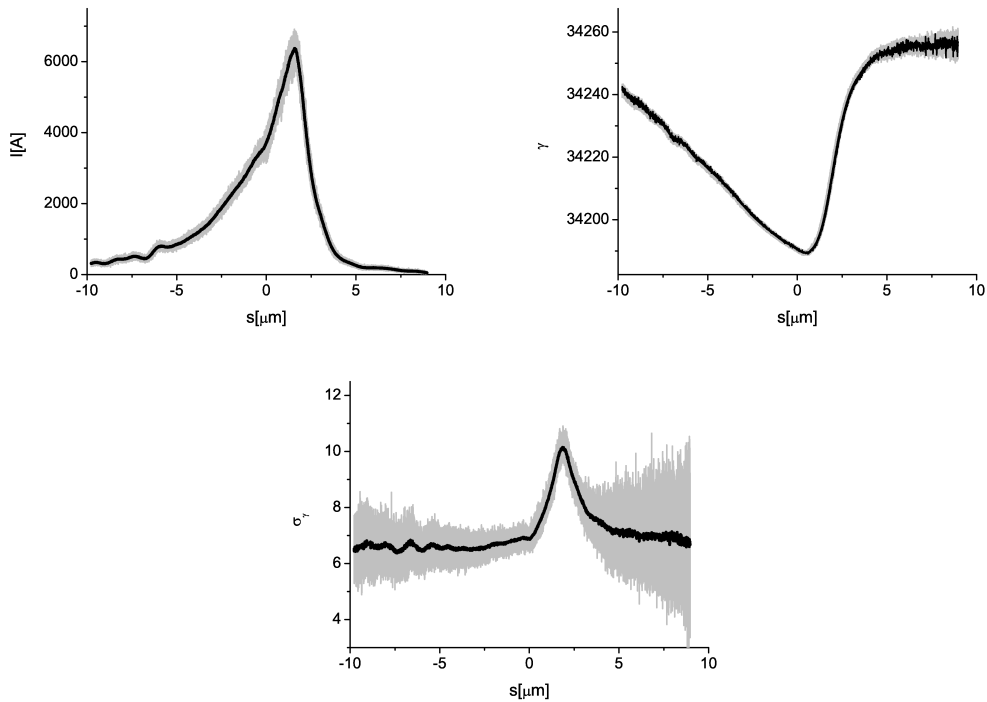


Fig. 21. Electron beam characteristics after the second magnetic chicane. (First Row, Left) Current profile. (First Row, Right) Energy profile along the beam. (Second Row) Electron beam energy spread profile.

Fig. 19 accordingly, to obtain the power and spectrum in Fig. 20. This power and spectrum are used for seeding.

Since we now deal with a conventional grating monochromator, the photon pulse is delayed with respect to the electron pulse. In our study case we assume a relatively large delay of about 1 ps. In order to compensate for such delay, one needs a chicane with a relatively large dispersion strength

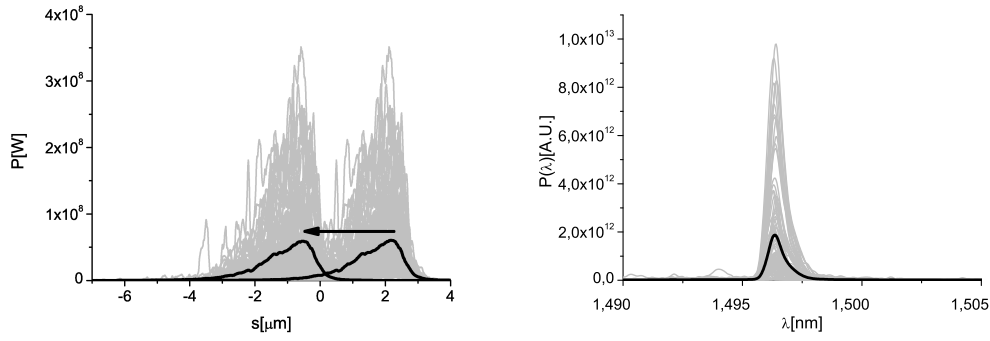


Fig. 22. Power and spectrum at the fundamental harmonic after the second chicane equipped with the X-ray optical delay line, delaying the radiation pulse with respect to the electron bunch. Grey lines refer to single shot realizations, the black line refers to the average over a hundred realizations.

$R_{56} \sim 0.6$ mm. In principle we cannot neglect the effects of the chicane dispersion on the electron bunch properties. We accounted for them with the help of the code Elegant [40], which was used to propagate the electron beam distribution through the chicane. Results are shown in Fig. 21.

Since the R_{56} is large enough to wash out the electron beam microbunching, we assume a fresh bunch at the entrance of the following undulator part constituted by 3 undulator cells. This means that the results in Fig. 21 are taken to generate a new beam file to be fed into GENESIS. The electron bunch is now seeded with the monochromatized radiation pulse in Fig. 20, so that the seed is amplified in the 3 undulator cells following the chicane. After that, the electron beam is sent through the second chicane, while the radiation pulse goes through the X-ray optical delay line described in Fig. 6, where the radiation pulse is delayed of about 6 fs with respect to the electron beam, as shown in Fig. 9. The power and spectrum of the radiation pulse after the optical delay line are shown in Fig. 22, where the combined effect of the optical delay and of the magnetic chicane is illustrated. This results in an overall delay of 6 fs. Note that the use of the mirror chicane also allows for an R_{56} in the order of ten microns. Thus, the combination of magnetic chicane and mirror chicane also allows for removing the electron microbunching produced in the second undulator.

Besides allowing for the installation of the optical delay line, which delays the radiation pulse of about half of the electron bunch size, the second chicane also smears out the microbunching in the electron bunch. As a result, at the entrance of the third undulator part the electron bunch can be considered as unmodulated, and half of it is seeded with the radiation pulse. The seeded half of the electron bunch amplifies the seed in the third undulator part, composed by four cells. The seeded part of the electron bunch is now spent, and its quality has deteriorated too much for further

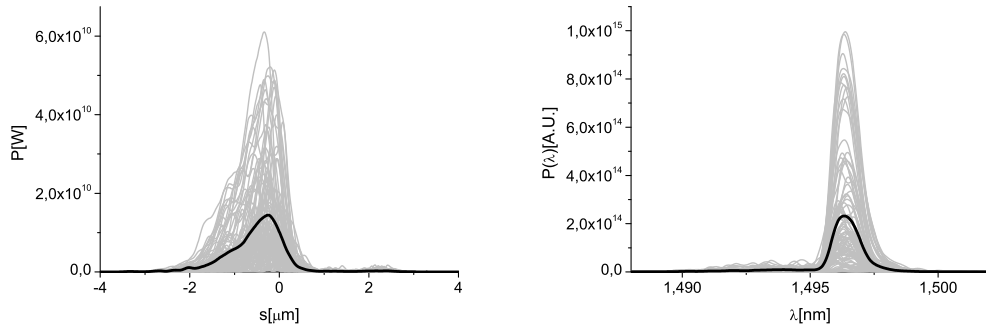


Fig. 23. Power and spectrum at the fundamental harmonic at the exit of the third undulator and before the third magnetic chicane. Grey lines refer to single shot realizations, the black line refers to the average over a hundred realizations.

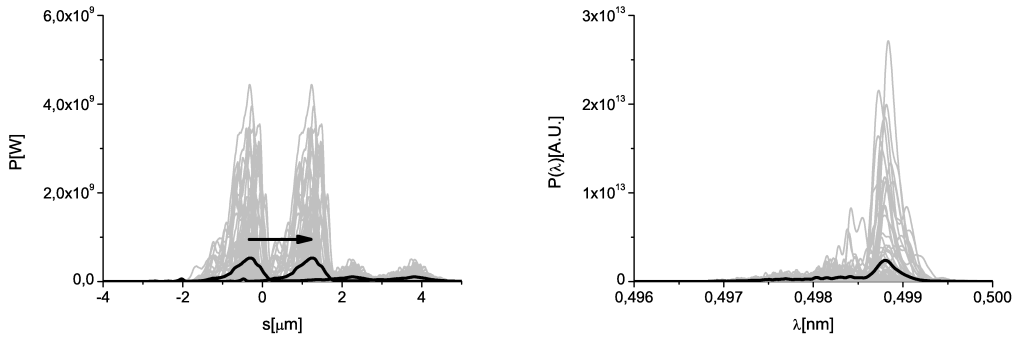


Fig. 24. Power and spectrum at the third harmonic after the third magnetic chicane. Grey lines refer to single shot realizations, the black line refers to the average over a hundred realizations.

lasing. After that, electrons and radiation are separated once more going through the third chicane. The hard X-ray self-seeding crystal is out, and the chicane simply acts as a delay line for the electron beam, which also smears out the microbunching. Power and spectrum following the third chicane are shown in Fig. 24.

By tuning the third chicane in the proper way, one can superimpose the radiation beam onto that part of the electron bunch that has not been seeded in the third undulator part. This is fresh, and can lase again in the fourth undulator part. Fig. 24 shows the effect of the magnetic chicane, which delays the electron bunch relative to the radiation pulse in order to allow for the seeding of the fresh part of the bunch. The radiation beam includes a relevant third-harmonic content, just slightly below the GW level as can be seen in Fig. 24, and is sufficient to act as a seed in the last part of the undulator. The fourth undulator part is not tuned at the fundamental harmonic, but rather at the third harmonic. This allows to reach the photon energy range between 2 keV and 3 keV.

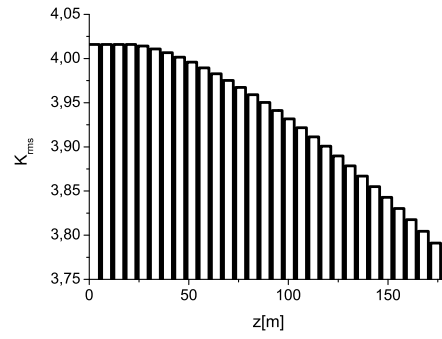


Fig. 25. Tapering law for the case $\lambda = 0.5$ nm.

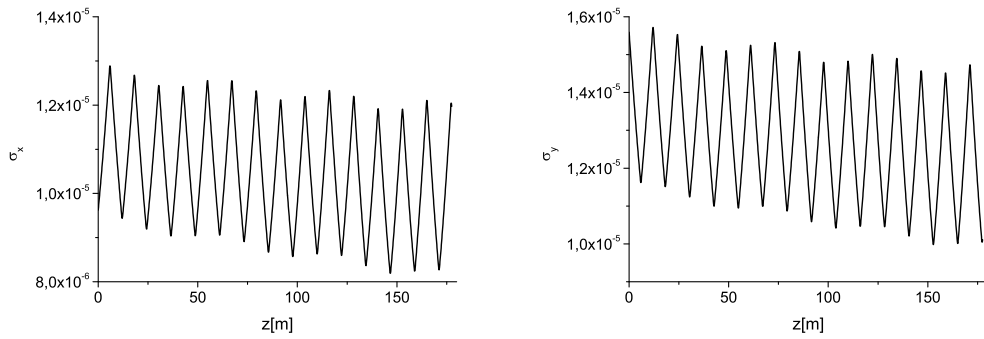


Fig. 26. Evolution of the horizontal (left plot) and vertical (right plot) dimensions of the electron bunch as a function of the distance inside the tapered part of the undulator at $\lambda = 0.5$ nm. The plots refer to the longitudinal position inside the bunch corresponding to the maximum current value. The quadrupole strength varies along the undulator, and is tuned for optimum output.

The fourth and last part of the undulator is composed by 29 cells, interrupted by a chicane which is switched off, and will be used in different energy ranges. The last undulator part is partly tapered post-saturation to allow for increasing the region where electrons and radiation interact properly to the advantage of the radiation pulse. Tapering is implemented by changing the K parameter of the undulator segment by segment according to Fig. 25. The tapering law used in this work has been implemented on an empirical basis, and the output has been optimized also by varying the quadrupole strength as shown in Fig. 26.

The use of tapering together with monochromatic radiation is particularly effective, since the electron beam does not experience brisk changes of the ponderomotive potential during the slippage process. The final output is presented in Fig. 27 in terms of power and spectrum. As one can see, simulations indicate an output power of about 2 TW.

The energy of the radiation pulse and the energy variance are shown in Fig.

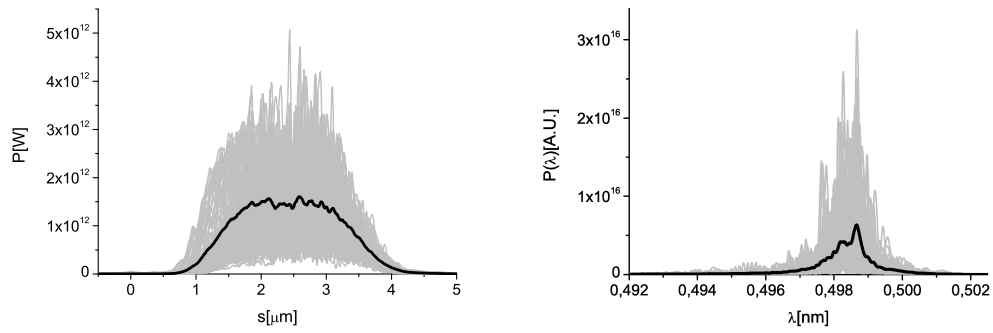


Fig. 27. Final output. Power and spectrum at the third harmonic after tapering. Grey lines refer to single shot realizations, the black line refers to the average over a hundred realizations.

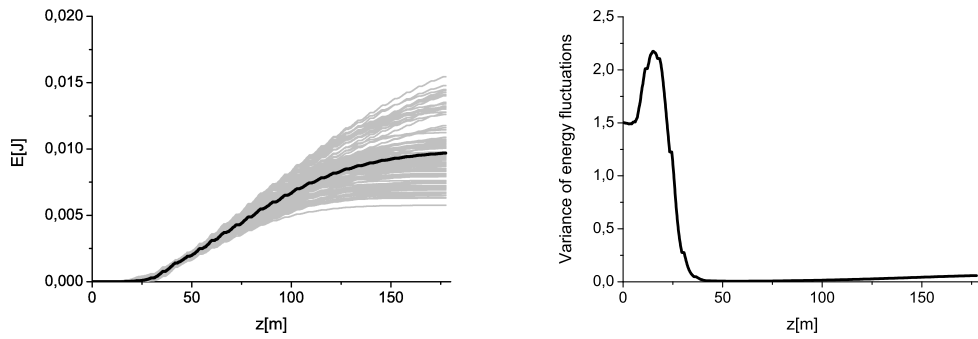


Fig. 28. Final output. Energy and energy variance of output pulses for the case $\lambda = 0.5$ nm. In the left plot, grey lines refer to single shot realizations, the black line refers to the average over a hundred realizations.

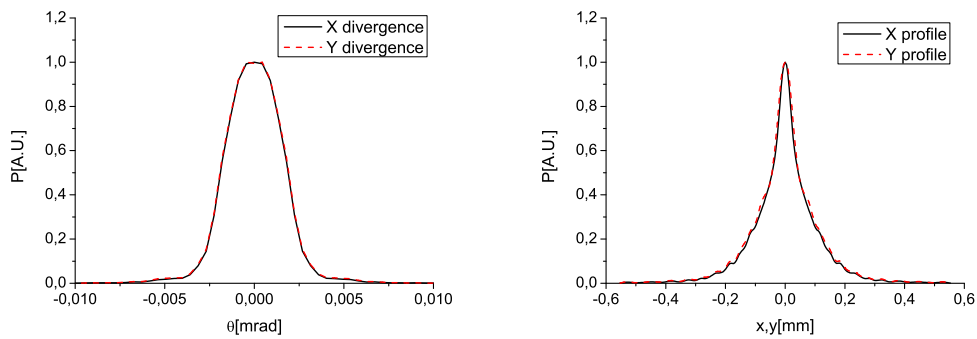


Fig. 29. Final output. X-ray radiation pulse energy distribution per unit surface and angular distribution of the X-ray pulse energy at the exit of output undulator for the case $\lambda = 0.5$ nm.

28 as a function of the position along the undulator. The divergence and the size of the radiation pulse at the exit of the final undulator are shown, instead, in Fig. 29. In order to calculate the size, an average of the transverse intensity profiles is taken. In order to calculate the divergence, the spatial

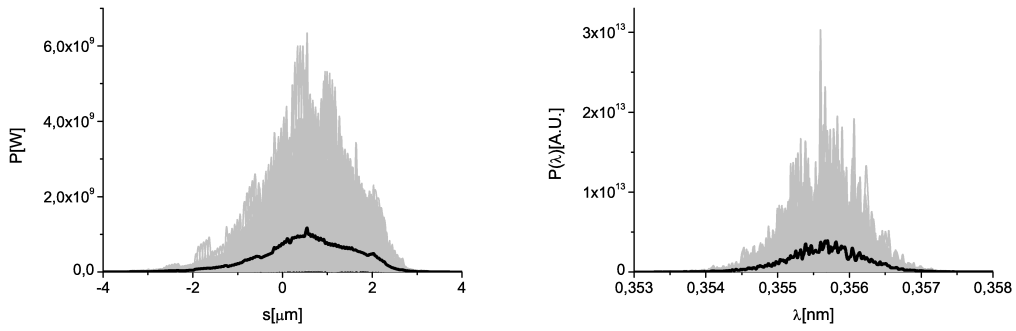


Fig. 30. Power and spectrum before the second magnetic chicane. Grey lines refer to single shot realizations, the black line refers to the average over a hundred realizations.

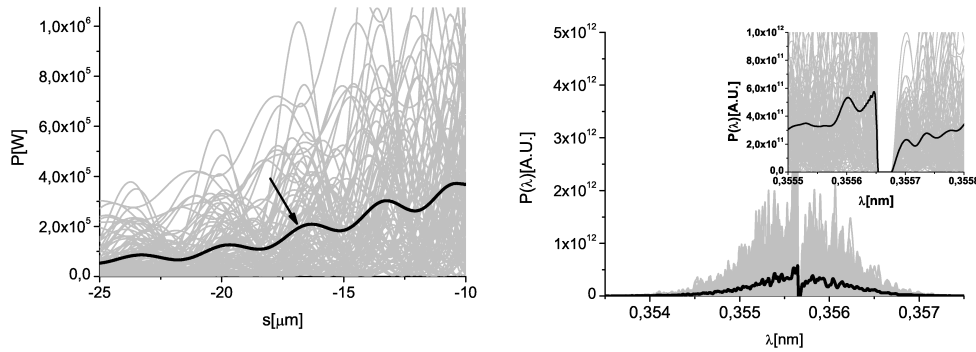


Fig. 31. Power and spectrum after the single crystal self-seeding X-ray monochromator. A 100 μm thick diamond crystal in Bragg transmission geometry (C(111) reflection, σ -polarization) is used. Grey lines refer to single shot realizations, the black line refers to the average over a hundred realizations. The black arrow indicates the seeding region.

Fourier transform of the field is calculated.

4.3 Photon energy range between 3 keV and 5 keV

We now consider generation of radiation in the photon energy between 3 keV and 5 keV, with reference to Fig. 11.

For this mode of operation, the first chicane is switched off, so that the first part of the undulator effectively consists of 7 uniform cells. We begin our investigation by simulating the SASE power and spectrum after the first part of the undulator, that is before the second magnetic chicane in the setup. Results are shown in Fig. 30.

The second magnetic chicane is switched on, and the single-crystal X-ray

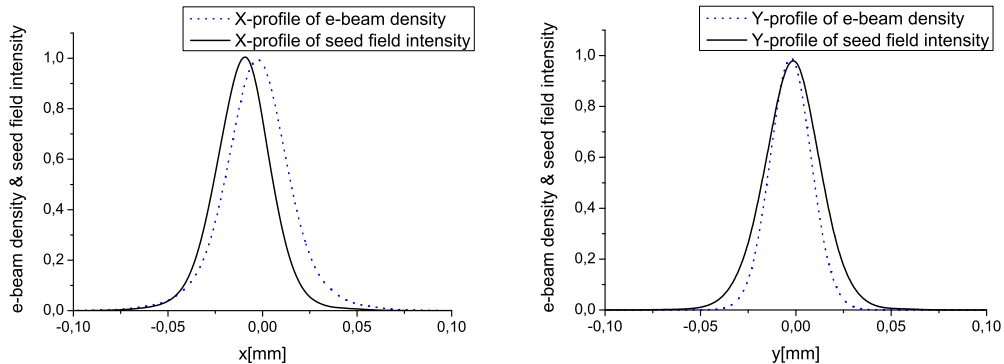


Fig. 32. Comparison between transverse profile of the seed field intensity and transverse profile of the electron beam density at the position used for seeding at $\lambda = 0.36$ nm. The plots refer to the longitudinal position inside the bunch corresponding to the maximum current value.

monochromator is set into the photon beam. For the 3 keV - 5 keV energy range we use a $100 \mu\text{m}$ -thick diamond crystal in Bragg transmission geometry. In particular, we take advantage of the C(111) reflection, σ -polarization. The crystal acts as a bandstop filter, and the output spectrum is plotted in Fig. 31 (right). Due to the bandstop effect, the signal in the time domain exhibits a long monochromatic tail, which is used for seeding, Fig. 31 (left). To this purpose, the electron bunch is slightly delayed by proper tuning of the magnetic chicane to be superimposed to the seeding signal.

It should be remarked that, according to Section 3, spatio-temporal coupling induced by the crystal monochromator should be accounted for in our study. In our simulations we calculate the temporal profile of the wake by convolving the incoming radiation pulse with the impulse response of the crystal. Since the incoming radiation pulse has a finite length, it follows that the average wake profile is different compared with the impulse response.

However, as concerns the inclusion of spatiotemporal coupling effects, we based our analysis on the result discussed in Section 3. This result was derived under the assumption that the incoming radiation pulse is a Dirac δ -function. In this case, our wake in the time domain simply coincides with the impulse response function of the crystal. The reason for such approximation can be explained by comparing the typical delay associated with the impulse response (about $20 \mu\text{m}$) with the pulse duration (about $3 \mu\text{m}$). From this comparison follows that we can neglect the length of the incoming pulse with accuracy of about 10% – 20%.

As already found in Section 3, the beam spot size is independent of time, but the beam central position changes as the pulse evolves in time. The transverse dependence of the electric field, in fact, obeys Eq. (6). We account

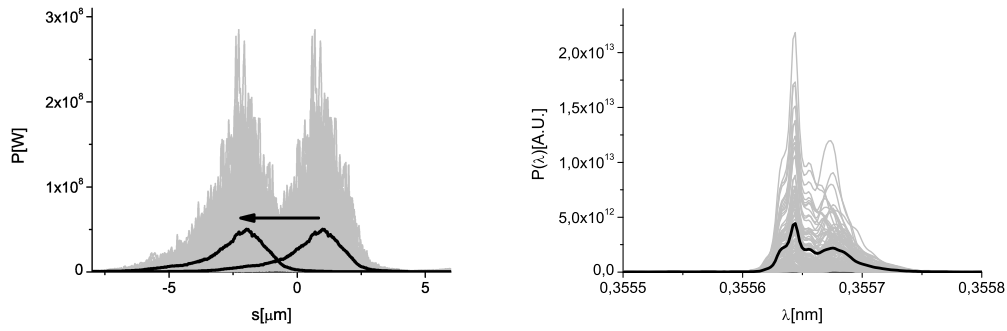


Fig. 33. Power and spectrum after the third chicane equipped with the X-ray optical delay line, delaying the radiation pulse with respect to the electron bunch. Grey lines refer to single shot realizations, the black line refers to the average over a hundred realizations.

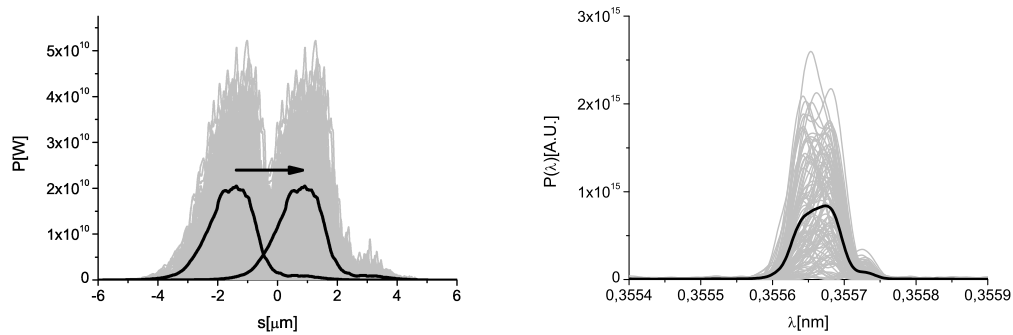


Fig. 34. Power and spectrum after the last magnetic chicane. Grey lines refer to single shot realizations, the black line refers to the average over a hundred realizations.

for this effect automatically in our simulations. A comparison between the transverse field profile used for seeding without accounting for the spatio-temporal coupling is shown in Fig. 32. This feature is accounted for in calculations.

Following the seeding setup, the electron bunch amplifies the seed in the following 4 undulator cells. After that, a third chicane is used to allow for the installation of an x-ray optical delay line, which retards the radiation pulse with respect to the electron bunch. The power and spectrum of the radiation pulse after the optical delay line are shown in Fig. 33, where the combined effect of the optical delay is illustrated.

Due to the presence of the optical delay, only part of the electron beam is used to further amplify the radiation pulse in the following 6 undulator cells. The electron beam part which has not lased is fresh, and can be used for further lasing. In order to do so, after amplification, the electron beam passes through the final magnetic chicane, which delays the electron beam. The power and spectrum of the radiation pulse after the last magnetic chicane

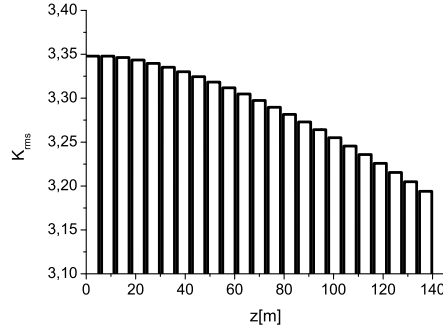


Fig. 35. Tapering law for the case $\lambda = 0.36$ nm.

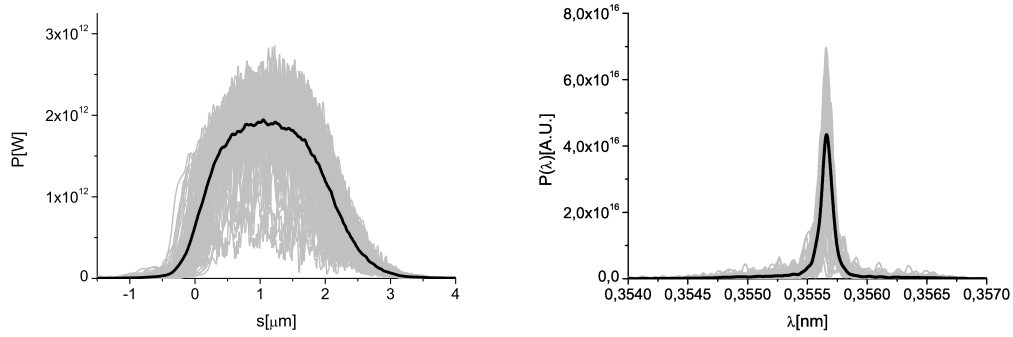


Fig. 36. Final output. Power and spectrum at the third harmonic after tapering. Grey lines refer to single shot realizations, the black line refers to the average over a hundred realizations.

are shown in Fig. 34. By delaying the electron bunch, the magnetic chicane effectively shifts forward the photon beam with respect to the electron beam. Tunability of such shift allows the selection of different photon pulse lengths. Moreover, an additional advantage of brought by the use of a fresh bunch technique in this mode of operation is the suppression of the intensity fluctuations of the seed down to 40% in the nonlinear regime before the last chicane. This suppression of fluctuations is useful in connection with the application of the tapering technique in the last part of the undulator. Fluctuations of the seed in the linear regime are, at variance, close to 100%.

The last part of the undulator is composed by 23 cells. It is partly tapered post-saturation, to increase the region where electrons and radiation interact properly to the advantage of the radiation pulse. Tapering is implemented by changing the K parameter of the undulator segment by segment according to Fig. 35. The tapering law used in this work has been implemented on an empirical basis.

The use of tapering together with monochromatic radiation is particularly effective, since the electron beam does not experience brisk changes of the ponderomotive potential during the slippage process. The final output is

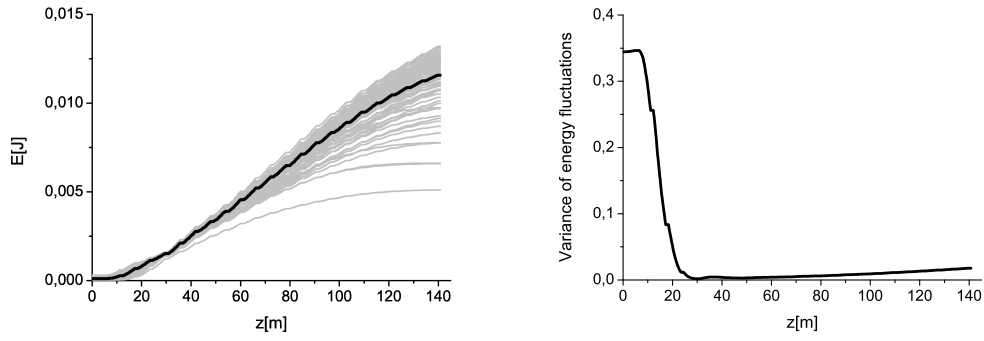


Fig. 37. Final output. Energy and energy variance of output pulses for the case $\lambda = 0.36$ nm. In the left plot, grey lines refer to single shot realizations, the black line refers to the average over a hundred realizations.

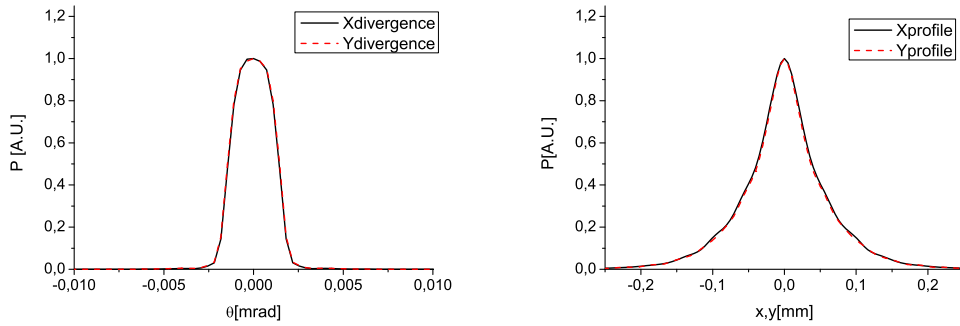


Fig. 38. Final output. X-ray radiation pulse energy distribution per unit surface and angular distribution of the X-ray pulse energy at the exit of output undulator for the case $\lambda = 0.36$ nm.

presented in Fig. 36 in terms of power and spectrum. As one can see, simulations indicate an output power of about 1.5 TW.

The energy of the radiation pulse and the energy variance are shown in Fig. 37 as a function of the position along the undulator. The divergence and the size of the radiation pulse at the exit of the final undulator are shown, instead, in Fig. 38. In order to calculate the size, an average of the transverse intensity profiles is taken. In order to calculate the divergence, the spatial Fourier transform of the field is calculated.

4.4 Photon energy range between 5 keV and 7 keV

Operation in the photon range between 5 keV and 7 keV will be possible by configuring the bio-imaging beamline as in Fig. 12. The configuration is very similar to the case for the range between 3 keV and 5 keV. The only difference is that the C(220) reflection is used instead of the C(111).

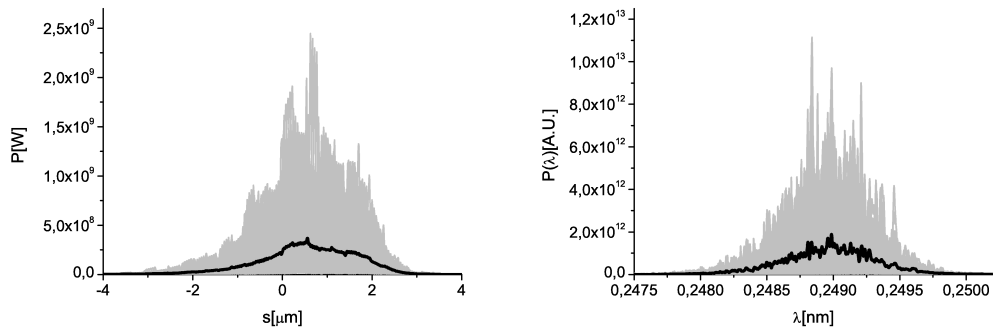


Fig. 39. Power and spectrum before the second magnetic chicane. Grey lines refer to single shot realizations, the black line refers to the average over a hundred realizations.

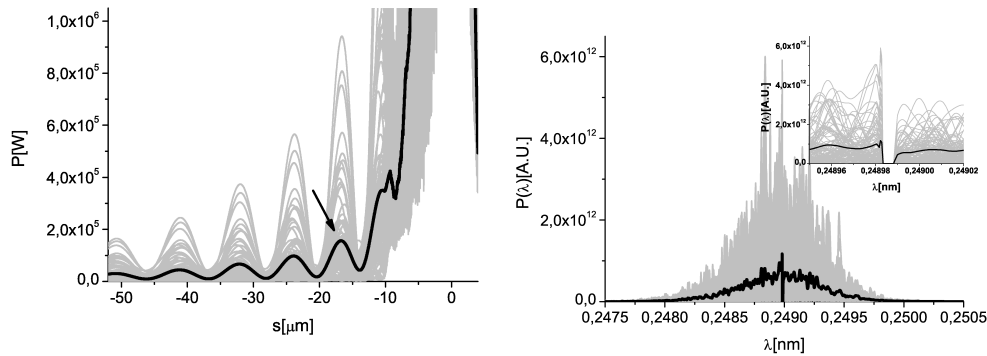


Fig. 40. Power and spectrum after the single crystal self-seeding X-ray monochromator. A 100 μm thick diamond crystal in Bragg transmission geometry (C(220) reflection, σ -polarization) is used. Grey lines refer to single shot realizations, the black line refers to the average over a hundred realizations. The black arrow indicates the seeding region.

As before, the first chicane is switched off, so that the first part of the undulator effectively consists of 7 uniform cells. We begin our investigation by simulating the SASE power and spectrum after the first part of the undulator, that is before the second magnetic chicane in the setup. Results are shown in Fig. 39.

The second magnetic chicane is switched on, and the single-crystal X-ray monochromator is set into the photon beam. For the 5 keV - 7 keV energy range we use a 100 μm -thick diamond crystal in Bragg transmission geometry. In particular, we take advantage of the C(220) reflection, σ -polarization, Fig. 40.

Following the seeding setup, the electron bunch amplifies the seed in the following 4 undulator cells. After that, a third chicane is used to allow for the installation of an x-ray optical delay line, which delays the radiation

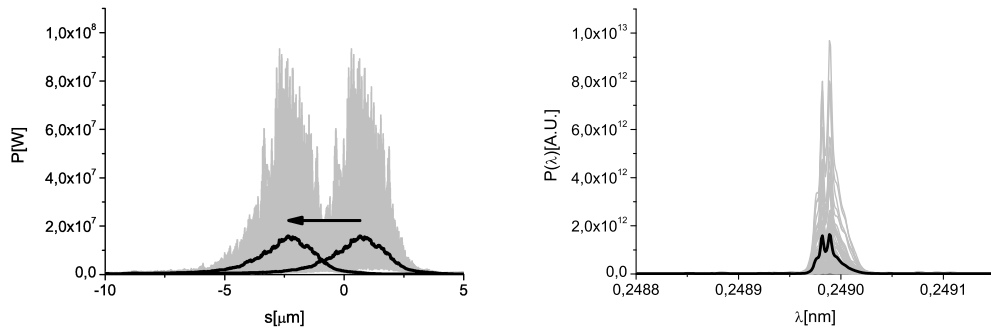


Fig. 41. Power and spectrum after the third chicane equipped with the X-ray optical delay line, delaying the radiation pulse with respect to the electron bunch. Grey lines refer to single shot realizations, the black line refers to the average over a hundred realizations.

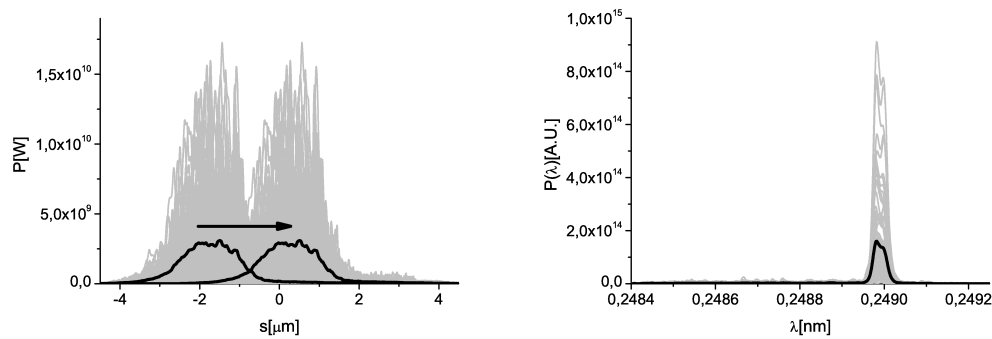


Fig. 42. Power and spectrum after the last magnetic chicane. Grey lines refer to single shot realizations, the black line refers to the average over a hundred realizations.

pulse with respect to the electron bunch. The power and spectrum of the radiation pulse after the optical delay line are shown in Fig. 41, where the effect of the optical delay is illustrated.

Due to the presence of the optical delay, only part of the electron beam is used to further amplify the radiation pulse in the following 6 undulator cells. The electron beam part which is not used is fresh, and can be used for further lasing. In order to do so, after amplification, the electron beam passes through the final magnetic chicane, which delays the electron beam. The power and spectrum of the radiation pulse after the last magnetic chicane are shown in Fig. 42. By delaying the electron bunch, the magnetic chicane effectively shifts forward the photon beam with respect to the electron beam. Tunability of such shift allows the selection of different photon pulse length.

The last part of the undulator is composed by 23 cells. It is partly tapered post-saturation, to increase the region where electrons and radiation interact properly to the advantage of the radiation pulse. Tapering is implemented by changing the K parameter of the undulator segment by segment according

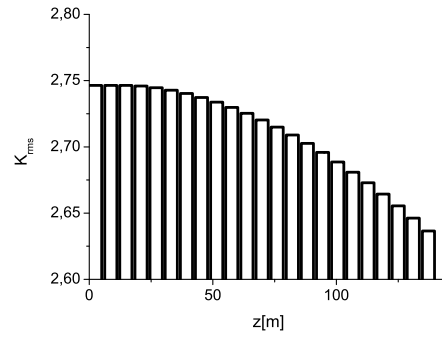


Fig. 43. Tapering law for the case $\lambda = 0.25$ nm.

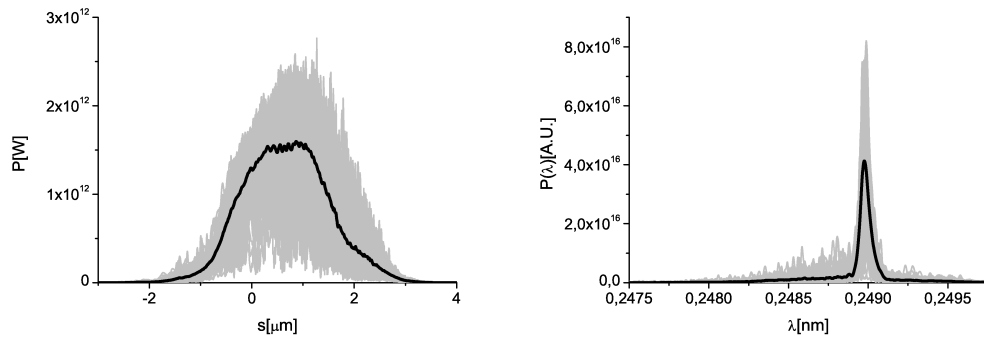


Fig. 44. Final output. Power and spectrum at the third harmonic after tapering. Grey lines refer to single shot realizations, the black line refers to the average over a hundred realizations.

to Fig. 43. The tapering law used in this work has been implemented on an empirical basis.

The use of tapering together with monochromatic radiation is particularly effective, since the electron beam does not experience brisk changes of the ponderomotive potential during the slippage process. The final output is presented in Fig. 44 in terms of power and spectrum. As one can see, simulations indicate an output power of about 1.5 TW.

The energy of the radiation pulse and the energy variance are shown in Fig. 45 as a function of the position along the undulator. The divergence and the size of the radiation pulse at the exit of the final undulator are shown, instead, in Fig. 46. In order to calculate the size, an average of the transverse intensity profiles is taken. In order to calculate the divergence, the spatial Fourier transform of the field is calculated.

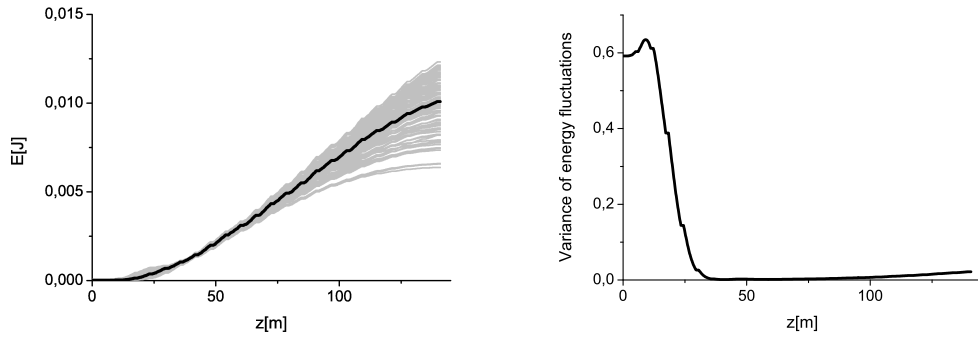


Fig. 45. Final output. Energy and energy variance of output pulses for the case $\lambda = 0.25$ nm. In the left plot, grey lines refer to single shot realizations, the black line refers to the average over a hundred realizations.

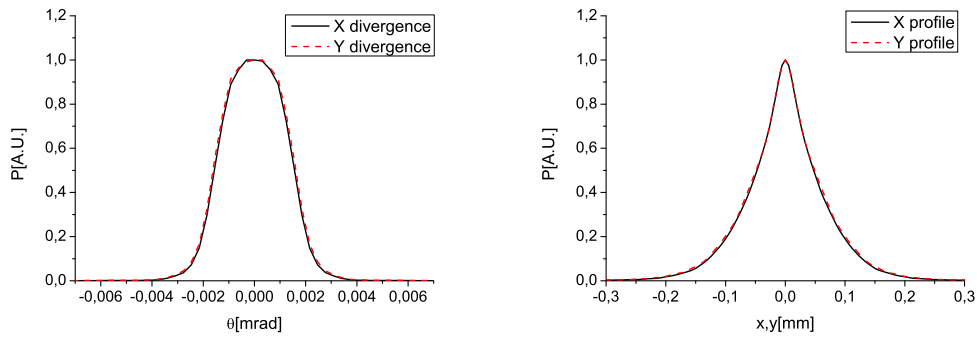


Fig. 46. Final output. X-ray radiation pulse energy distribution per unit surface and angular distribution of the X-ray pulse energy at the exit of output undulator for the case $\lambda = 0.25$ nm.

4.5 Photon energy range between 7 keV and 9 keV

We now consider the photon energy range between 7 keV and 9 keV. In this case the beamline will be configured as in Fig. 13. A feasibility study dealing with this energy range can be found in [6].

4.6 Photon energy range between 9 keV and 13 keV

Finally, we consider generation of radiation in the photon energy between 9 keV and 13 keV. The undulator line will be configured as in Fig. 11, the only difference now being that the final 23 cells will be tuned at the third harmonic of the fundamental, thus allowing to reach the photon energy between 9 keV and 13 keV.

For this mode of operation, the first chicane is switched off, so that the first

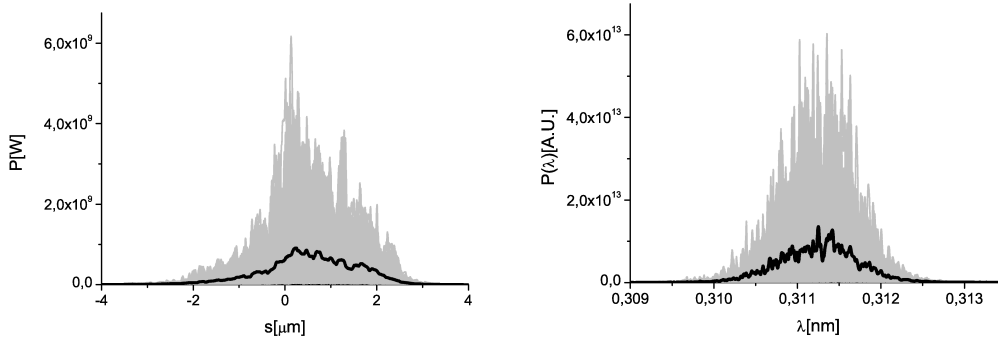


Fig. 47. Power and spectrum before the second magnetic chicane. Grey lines refer to single shot realizations, the black line refers to the average over a hundred realizations.

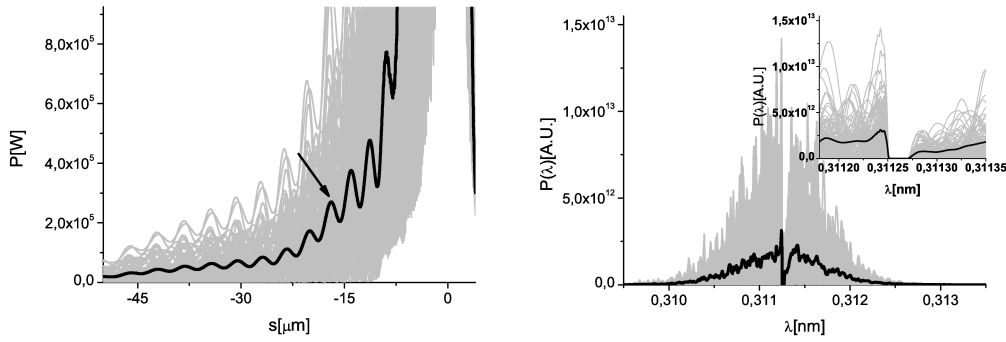


Fig. 48. Power and spectrum after the single crystal self-seeding X-ray monochromator. A 100 μm thick diamond crystal in Bragg transmission geometry (C(111) reflection, σ -polarization) is used. Grey lines refer to single shot realizations, the black line refers to the average over a hundred realizations. The black arrow indicates the seeding region.

part of the undulator effectively consists of 7 uniform cells. We begin our investigation by simulating the SASE power and spectrum after the first part of the undulator, that is before the second magnetic chicane in the setup. Results are shown in Fig. 47.

The second magnetic chicane is switched on, and the single-crystal X-ray monochromator is set into the photon beam. Since we want to generate radiation in the 3 keV - 4 keV energy range, we use a 100 μm -thick diamond crystal in Bragg transmission geometry. In particular, we take advantage of the C(111) reflection, σ -polarization. The crystal acts as a bandstop filter, and the output spectrum is plotted in Fig. 48 (right). Due to the bandstop effect, the signal in the time domain exhibits a long monochromatic tail, which is used for seeding, Fig. 48 (left). To this purpose, the electron bunch is slightly delayed by proper tuning of the magnetic chicane to be superimposed to the seeding signal. The difference with respect to Fig. 31 is in a slightly

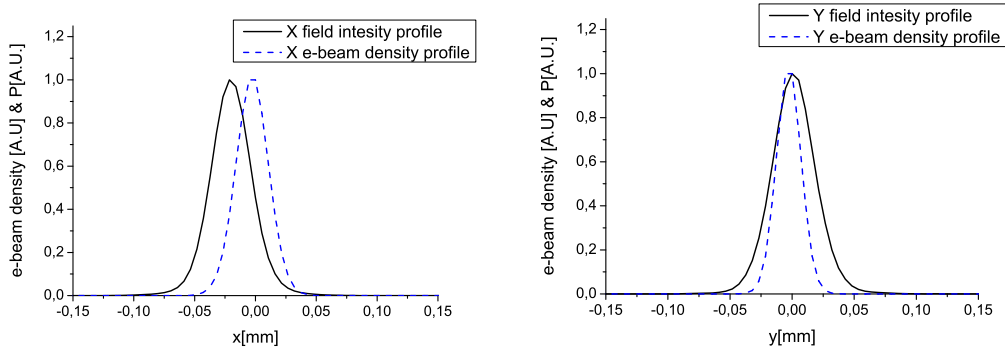


Fig. 49. Comparison between transverse profile of the seed field intensity and transverse profile of the electron beam density at the position used for seeding at $\lambda = 0.3$ nm. The plots refer to the longitudinal position inside the bunch corresponding to the maximum current value.

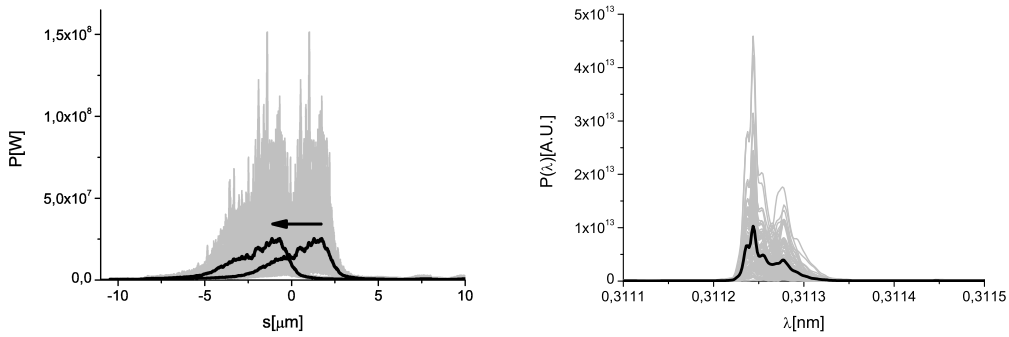


Fig. 50. Power and spectrum after the third chicane equipped with the X-ray optical delay line, delaying the radiation pulse with respect to the electron bunch. Grey lines refer to single shot realizations, the black line refers to the average over a hundred realizations.

different frequency, since in this Section we want to study the feasibility of production of 12 keV radiation.

As before it should be remarked that, according to Section 3, spatio-temporal coupling induced by the crystal monochromator should be accounted for in our study. A comparison between the electron beam position and the photon beam position after the crystal is shown in Fig. 49. The shift difference is due to the spatio-temporal coupling induced by the crystal, and must be accounted for in calculations. The longitudinal position at which Fig. 49 refers is that of the seeding peak, compared to the lasing part of the bunch.

Following the seeding setup, the electron bunch amplifies the seed in the following 4 undulator cells. After that, a third chicane is used to allow for the installation of an x-ray optical delay line, which retards the radiation pulse with respect to the electron bunch. The power and spectrum of the

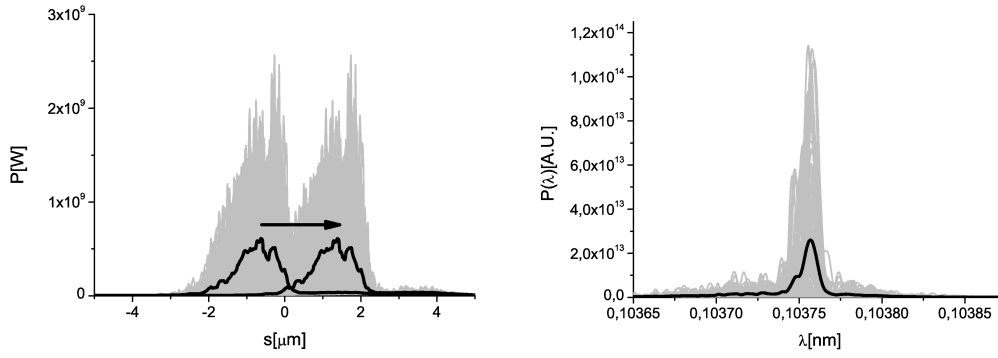


Fig. 51. Power and spectrum after the last magnetic chicane. Grey lines refer to single shot realizations, the black line refers to the average over a hundred realizations.

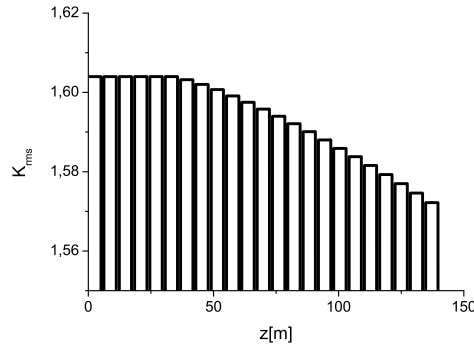


Fig. 52. Tapering law for the case $\lambda = 0.1$ nm.

radiation pulse after the optical delay line are shown in Fig. 50, where the effect of the optical delay is illustrated.

Due to the presence of the optical delay, only part of the electron beam is used to further amplify the radiation pulse in the following 6 undulator cells. The electron beam part which has not lased is fresh, and can be used for further lasing. In order to do so, after amplification, the electron beam passes through the final magnetic chicane, which delays the electron beam. During the previous amplification, a consistent amount of bunching at the third harmonic of the fundamental is produced. The power and spectrum of the radiation pulse at the third harmonic after the last magnetic chicane are shown in Fig. 51. By delaying the electron bunch, the magnetic chicane effectively shifts forward the photon beam with respect to the electron beam. Tunability of such shift allows the selection of different photon pulse lengths.

The last part of the undulator is composed by 23 cells. It is tuned at the third harmonic of the fundamental, i.e. around 12 keV in our case, and partly tapered post-saturation, to increase the region where electrons and radiation interact properly to the advantage of the radiation pulse. Tapering

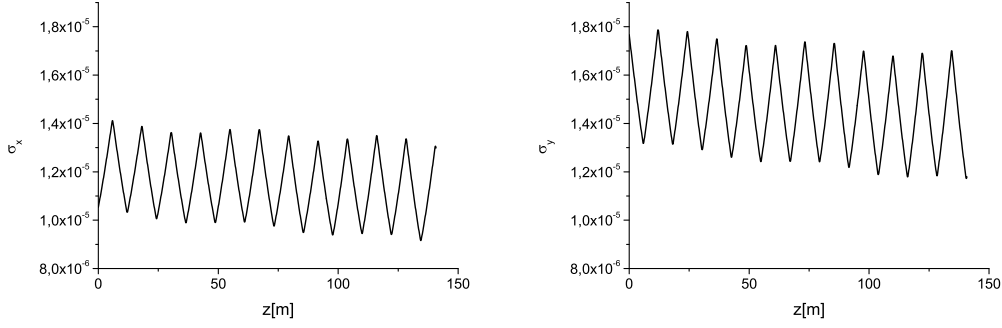


Fig. 53. Evolution of the horizontal (left plot) and vertical (right plot) dimensions of the electron bunch as a function of the distance inside the tapered part of the undulator at $\lambda = 0.1$ nm. The plots refer to the longitudinal position inside the bunch corresponding to the maximum current value. The quadrupole strength is varied along the undulator axis in order to optimize the output.

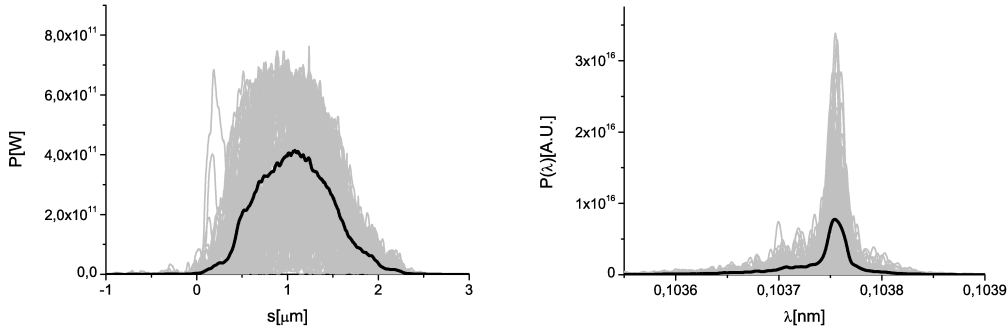


Fig. 54. Final output. Power and spectrum at the third harmonic after tapering. Grey lines refer to single shot realizations, the black line refers to the average over a hundred realizations.

is implemented by changing the K parameter of the undulator segment by segment according to Fig. 52. The tapering law used in this work has been implemented on an empirical basis, and the output has been optimized also by varying the quadrupole strength as shown in Fig. 53.

As usual, combining tapering with monochromatic radiation generation is particularly effective, since the electron beam does not experience brisk changes of the ponderomotive potential during the slippage process. The final output is presented in Fig. 54 in terms of power and spectrum. As one can see, simulations indicate an output power of about 0.5 TW.

The energy of the radiation pulse and the energy variance are shown in Fig. 55 as a function of the position along the undulator. The divergence and the size of the radiation pulse at the exit of the final undulator are shown, instead, in Fig. 56. In order to calculate the size, an average of the transverse intensity profiles is taken. In order to calculate the divergence, the spatial

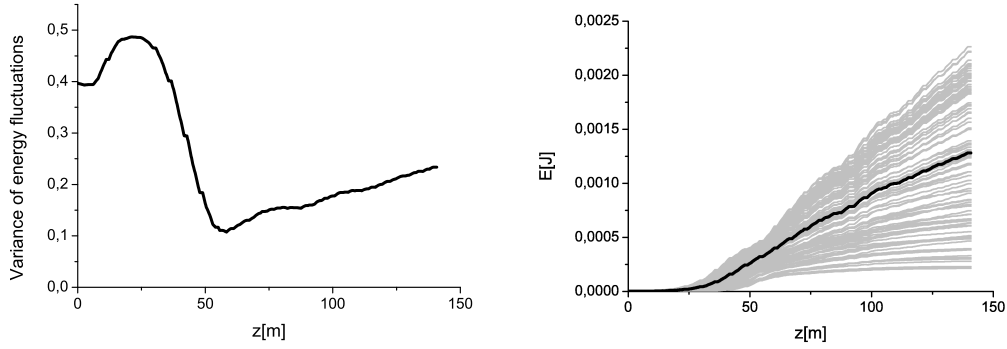


Fig. 55. Final output. Energy and energy variance of output pulses for the case $\lambda = 0.1$ nm. In the left plot, grey lines refer to single shot realizations, the black line refers to the average over a hundred realizations.

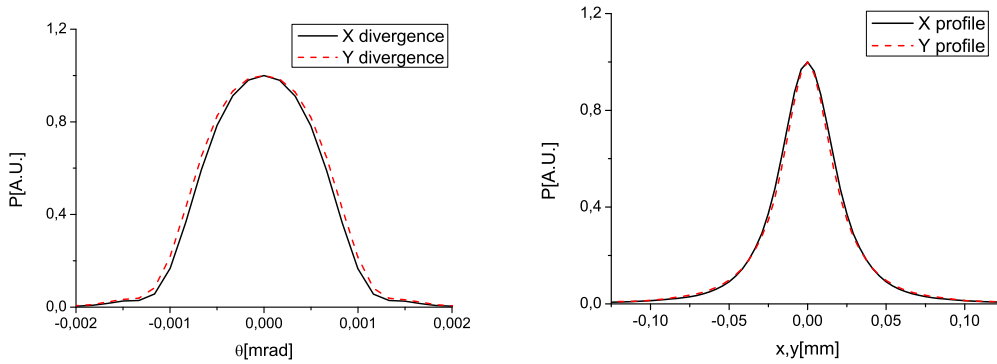


Fig. 56. Final output. X-ray radiation pulse energy distribution per unit surface and angular distribution of the X-ray pulse energy at the exit of output undulator for the case $\lambda = 0.1$ nm.

Fourier transform of the field is calculated.

5 Conclusions

The highest priority for bioimaging experiments at any advanced XFEL facility is to establish a dedicated beamline for studying biological objects at the mesoscale, including large macromolecules, macromolecular complexes, and cell organelles. This requires 2 keV - 6 keV photon energy range and TW peak power pulses. However, higher photon energies are needed to reach anomalous edges of commonly used elements (such as Se) for anomalous experimental phasing. Studies at intermediate resolutions need access to the water window [5].

A conceptual design of a dedicated bio-imaging beamline based on the

self-seeding scheme developed for European XFEL was suggested in [6]. The critical attribute of the proposed beamline, compared with the baseline SASE1 and SASE2 beamlines, is a wider photon energy range that spans from the water window up to the K-edge of Selenium (12.6 keV). With the current design of the European XFEL, the most preferable photon energy range between 3 keV and 5 keV cannot be used for biological scattering experiments, but the new proposed beamline could fill this gap operating at those energies with TW peak power.

The first goal in developing a design for a dedicated bio-imaging beamline is to make it satisfying all requirements. Once that is done, the next step is to optimize the design, making it as simple as possible. In order to improve the original design, here we propose to extend the photon energy range of the self-seeding setup with single crystal monochromator to lower photon energies down to 3 keV. An important aspect of this extension is that the self-seeding scheme with single crystal monochromator is now routinely used in generating of narrow bandwidth X-ray pulses at the LCLS [47]. It combines a potentially wide photon energy range with a much needed experimental simplicity. Only one X-ray optical element is needed, and no sensitive alignment is required. The range of applicability of this novel method is a slightly limited, at present, by the availability of a short pulse duration (of about 10 fs or less). However, this range nicely matches that for single biomolecule imaging.

Optimization of the bio-imaging beamline is performed with extensive start-to-end simulations, which also take into account effects such as the spatiotemporal coupling caused by the single crystal monochromator. One must keep this effect in mind when performing the design of any self-seeding setup. The spatial shift is proportional to $\cot(\theta_B)$, and is therefore maximal in the range for small Bragg angles θ_B . A Bragg geometry close to backscattering (i.e. θ_B close to $\pi/2$) would be a more advantageous option from this viewpoint, albeit with a decrease in the spectral tunability [43, 45]. It is worth mentioning that this distortion is easily suppressed by the right choice of crystals within the photon energy range between 3 keV and 9 keV. Here we propose to use a set of three diamond crystals. For the C(111), the C(220) and the C(400) Bragg reflections (σ -polarization), it will be possible to respectively cover the photon energy ranges 3 keV - 5 keV, 5 keV - 7 keV, and 7 keV - 9 keV. Finding a solution suitable for the spectral range between 9 keV and 13 keV is major challenge due to the large value of $\cot(\theta_B)$ for the C(400) reflection case. Fortunately, even in this case, this obstacle can be overcome by using a fresh bunch technique, and exploiting the self-seeding setup with a C(111) single crystal monochromator, which is tunable in the photon energy range around 4 keV, in combination with harmonic generation techniques.

The goal of the present optimized proposal for a dedicated bio-imaging beamline presented here is to aim for experimental simplification and performance improvement. The design electron energy in the most preferable spectral range 3 keV - 5 keV is increased up to 17.5 GeV. The peak power is shown to reach a maximum value of 2 TW. The new design takes additional advantage of the fact that 17.5 GeV is the most preferable operation energy for the SASE1 and the SASE2 beamlines. Because of this, the optimized beamline is not sensitive to the parallel operation with other European XFEL beamlines.

6 Acknowledgements

We are grateful to Massimo Altarelli, Reinhard Brinkmann, Henry Chapman, Janos Hajdu, Viktor Lamzin, Serguei Molodtsov and Edgar Weckert for their support and their interest during the compilation of this work.

References

- [1] J. Hajdu, *Curr. Opin. Struct. Biol.* 10, 569 (2000)
- [2] R. Neutze et al., *Nature* 406, 752 (2000)
- [3] K. J. Gaffney and H. N. Chapman, *Science* 316, 1444 (2007)
- [4] M. M. Seibert et al., *Nature* 470 (7332) 78-81 (2011)
- [5] S. Baradaran et al., *LCLS-II New Instruments Workshops Report*, SLAC-R-993 (2012), see Section 4.3.2. by H. Chapman et al., and Section 4.3.3. by F. R. N. C. Maia et al.
- [6] G. Geloni, V. Kocharyan and E. Saldin, "Conceptual design of an undulator system for a dedicated bio-imaging beamline at the European X-ray FEL", DESY 12-082, <http://arxiv.org/abs/1205.6345> (2012).
- [7] A. Lin and J.M. Dawson, *Phys. Rev. Lett.* 42 2172 (1986)
- [8] P. Sprangle, C.M. Tang and W.M. Manheimer, *Phys. Rev. Lett.* 43 1932 (1979)
- [9] N.M. Kroll, P. Morton and M.N. Rosenbluth, *IEEE J. Quantum Electron.*, QE-17, 1436 (1981)
- [10] T.J. Orzechowski et al., *Phys. Rev. Lett.* 57, 2172 (1986)
- [11] W. Fawley et al., *NIM A* 483 (2002) p 537
- [12] M. Cornacchia et al., *J. Synchrotron rad.* (2004) 11, 227-238
- [13] X. Wang et al., *PRL* 103, 154801 (2009)
- [14] J. Feldhaus et al., *Optics. Comm.* 140, 341 (1997).
- [15] E. Saldin, E. Schneidmiller, Yu. Shvyd'ko and M. Yurkov, *NIM A* 475 357 (2001).
- [16] E. Saldin, E. Schneidmiller and M. Yurkov, *NIM A* 445 178 (2000).

- [17] R. Treusch, W. Brefeld, J. Feldhaus and U Hahn, Ann. report 2001 "The seeding project for the FEL in TTF phase II" (2001).
- [18] A. Marinelli et al., Comparison of HGHG and Self Seeded Scheme for the Production of Narrow Bandwidth FEL Radiation, Proceedings of FEL 2008, MOPPH009, Gyeongju (2008).
- [19] G. Geloni, V. Kocharyan and E. Saldin, "Scheme for generation of highly monochromatic X-rays from a baseline XFEL undulator", DESY 10-033 (2010).
- [20] Geloni, G., Kocharyan V., and Saldin, E., "A novel Self-seeding scheme for hard X-ray FELs", Journal of Modern Optics, vol. 58, issue 16, pp. 1391-1403, DOI:10.1080/09500340.2011.586473 (2011)
- [21] G. Geloni, V. Kocharyan and E. Saldin, "Scheme for generation of fully coherent, TW power level hard x-ray pulses from baseline undulators at the European XFEL", DESY 10-108 (2010).
- [22] Geloni, G., Kocharyan, V., and Saldin, E., "Production of transform-limited X-ray pulses through self-seeding at the European X-ray FEL", DESY 11-165 (2011).
- [23] W.M. Fawley et al., Toward TW-level LCLS radiation pulses, TUOA4, to appear in the FEL 2011 Conference proceedings, Shanghai, China, 2011
- [24] J. Wu et al., Simulation of the Hard X-ray Self-seeding FEL at LCLS, MOPB09, to appear in the FEL 2011 Conference proceedings, Shanghai, China, 2011
- [25] Y. Jiao et al. Phys. Rev. ST Accel. Beams 15, 050704 (2012)
- [26] I Ben-Zvi and L. H. Yu, Nucl. Instr. and Methods, A 393, 96 (1997).
- [27] Y. Ding, Z. Huang and R. Ruth, Phys.Rev.ST Accel.Beams, vol. 13, p. 060703 (2010).
- [28] G. Geloni, V. Kocharyan and E. Saldin, "A simple method for controlling the line width of SASE X-ray FELs", DESY 10-053 (2010).
- [29] Geloni, G., Kocharyan, V., and Saldin, E., "Cost-effective way to enhance the capabilities of the LCLS baseline", DESY 10-133 (2010).
- [30] J. Wu et al., "Staged self-seeding scheme for narrow bandwidth , ultra-short X-ray harmonic generation free electron laser at LCLS", proceedings of 2010 FEL conference, Malmo, Sweden, (2010).
- [31] I. Zagorodnov, "Beam Dynamics Simulations for XFEL", <http://www.desy.de/xfel-beam/s2e> (2011).
- [32] G. Geloni, V. Kocharyan and E. Saldin, "Extension of self-seeding scheme with single crystal monochromator to lower energy < 5 keV as a way to generate multi-TW scale pulses at the European XFEL ", DESY 12-121, <http://arxiv.org/abs/1207.1981> (2012).
- [33] Y. Feng et al., "System design for self-seeding the LCLS at soft X-ray energies", to appear in the Proceedings of the 24th International FEL Conference, Nara, Japan (2012).
- [34] Y. Feng, J. Hastings, P. Heimann, M. Rowen, J. Krzywinski, and J. Wu, "X-ray Optics for soft X-ray self-seeding the LCLS-II", proceedings of

- 2010 FEL conference, Malmo, Sweden, (2010).
- [35] Y. Feng, P. Heimann, J. Wu, J. Krzywinski, M. Rowen, and J. Hastings, "Compact Grating Monochromator Design for LCLS-I Soft X-ray Self-Seeding", https://slacportal.slac.stanford.edu/sites/lcls_public/lcls_ii/Lists/LCLS.II_Calendar/Physics_Meetings.aspx, May 2011 and <https://sites.google.com/a/lbl.gov/realizing-the-potential-of-seeded-fels-in-the-soft-x-ray-regime-workshop/talks>, October 2011
 - [36] P. Emma et al., Nature photonics doi:10.1038/nphoton.2010.176 (2010)
 - [37] Geloni, G., Kocharyan, V., and Saldin, E., "Self-seeding scheme for the soft X-ray line at the European XFEL", DESY 12-034 (2012).
 - [38] R. Brinkmann, E. Schnedmiller and M. Yurkov, DESY 10-011(2010) and
 - [39] F. J. Decker, et al., Multiple FELs from the one LCLS Undulator, THPB31, Proceedings of the 33rd FEL conference, Shanghai, China, 2011 to be published.
 - [40] M. Borland, http://www.aps.anl.gov/Accelerator_Systems_Division/Accelerator_Operations_Physics/software.shtml#elegant
 - [41] M. Altarelli, et al. (Eds.) XFEL, The European X-ray Free-Electron Laser, Technical Design Report, DESY 2006-097, Hamburg (2006).
 - [42] W. Decking, "Possible Undulator System Length" 06.07.2012 (Internal DESY technical note available on special request only).
 - [43] R. R Lindberg and Y. V. Shvyd'ko, "Time dependence of Bragg forward scattering and self-seeding of hard x-ray free-electron lasers", <http://arxiv.org/abs/1202.1472>
 - [44] P. Gabolde et al., "Describing first-order spatio-temporal distortions in ultrashort pulses using normalized parameters", Optics Express 15, 242 (2007)
 - [45] G. Geloni, V. Kocharyan and E. Saldin, "Pulse-front tilt caused by the use of a grating monochromator and self-seeding of soft X-ray FELs", DESY 12-051, <http://arxiv.org/abs/1203.6442> (2012).
 - [46] S Reiche et al., Nucl. Instr. and Meth. A 429, 243 (1999).
 - [47] J. Amann et al., Nature Photonics, DOI: 10.1038/NPHOTON.2012.180 (2012).